Applied Thermal Engineering 302 (2026) 131854

Contents lists available at ScienceDirect

Applied Thermal Engineering

journal homepage: www.elsevier.com/locate/apthermeng

Research Paper

Thermal performance evaluation of a parabolic trough solar collector with helical and trapezoidal Turbulators: Experimental, CFD, and AI-based analysis

Mehmet DAS [a,*], Murat Catalkaya [b], Oguzhan Pektezel [c], Mithat Simsek [d]

[a] Mechanical Engineering Department, Engineering Faculty, Firat University, 23100, Elazig, Türkiye
[b] Vocational school of technical sciences, Kahramanmaras Sutcu imam University, 46100, K. Maraş, Türkiye
[c] Mechanical Engineering Department, Balikesir University, 10145, Balıkesir, Türkiye
[d] Mechanical Engineering Department, Tokat Gaziosmanpasa University, 60250, Tokat, Türkiye

ARTICLE INFO

Keywords:
Parabolic trough solar collector
Turbulator
Computational fluid dynamics
Exergy analysis
M5P model tree
Elastic.Net regression

ABSTRACT

Parabolic trough solar collectors (PTC) offer notable potential for solar thermal applications, but performance is hindered by limited convective heat transfer within the receiver tube. This research proposes an integrated experimental, three-dimensional computational fluid dynamics (CFD), and explainable AI framework to evaluate PTCs with helical and trapezoidal turbulators. The central contribution is the experimentally validated combination of CFD analysis and AI-based temperature prediction for PTCs with internal turbulator geometries. Outdoor experiments under Tokat climatic conditions validated the CFD model using measured outlet-temperature data during a stable period with solar radiation near 900 W/m^2 and outlet temperature of 140–150 °C. The CFD and experimental results are closely aligned, with mean absolute error (MAE) and root mean square error (RMSE) both around 0.85. Turbulators enhanced fluid mixing and outlet temperature compared to a reference tube; the helical turbulator increased outlet temperature by 7–9%, and the trapezoidal by 3–5%. Correspondingly, annual energy output rose from 546.9 kWh/year (reference) to 694.6 kWh/year (helical) and 661.8 kWh/year (trapezoidal), with CO_2 emissions reductions reaching 0.283 ton/year for the helical design. The M5P and Elastic.Net regression models achieved R^2 scores of 0.95 and 0.90, respectively, for outlet temperature prediction using environmental parameters. This study demonstrates that the helical turbulator is the most effective configuration in terms of outlet-temperature enhancement under the investigated operating conditions, and that the combined experimental–CFD–AI approach provides an actionable, interpretable tool for improving air-based PTC systems used in thermal applications such as process-air heating and potential drying-related systems.

1. Introduction

The rapid increase in industrialization and urbanization, the rise in atmospheric carbon emissions, and the depletion of fossil fuel reserves have made it imperative to turn to alternative renewable energy sources; in this context, solar energy stands out as one of the most promising. Among solar energy conversion systems, Parabolic Trough Collectors (PTC) represent the most mature, robust, and widely used linear concentrator technology for thermal energy generation in commercial and industrial applications and are used in many areas, such as drying, cooling, and heating [1]. PTC use parabolic mirrors to focus sunlight onto a cylindrical receiver tube, through which a Heat Transfer Fluid (HTF) circulates. These systems enable high outlet temperatures (500 °C or higher) for electricity generation and process heat [2].

The main components of CSP systems are the receiver tube (absorber), heat transfer fluid, and reflective mirror. Improving the overall performance of these collectors requires enhancing the performance of key components, starting with the tube collector itself, the HTF properties, the optical design, and the integration of thermal energy storage systems [3]. However, PTC still face significant challenges [4]. The large collector surface area leads to radiation and convection losses, while the naturally non-homogeneous distribution of solar flux on the collector tube can cause thermal stresses, optical losses, and degradation

* Corresponding author.
E-mail addresses: m.das@firat.edu.tr (M. DAS), muratcatalkaya@ksu.edu.tr (M. Catalkaya), oguzhan.pektezel@balikesir.edu.tr (O. Pektezel), mithat.simsek@gop.edu.tr (M. Simsek).

https://doi.org/10.1016/j.applthermaleng.2026.131854
Received 18 February 2026; Received in revised form 24 May 2026; Accepted 5 June 2026
Available online 9 June 2026
1359-4311/

Nomenclature

Symbol and abbreviation

AI	Artificial intelligence	–
ANN	Artificial neural network	–
CFD	Computational fluid dynamics	–
CSP	Concentrated solar power	–
DNI	Direct normal irradiance	W/m^2
DT	Decision tree	–
Elastic.Net	Regularized regression model combining L1 and L2 penalties	–
GHI	Global horizontal irradiance	W/m^2
HTF	Heat transfer fluid	–
MAE	Mean absolute error	°C
M5P	Model tree algorithm combining decision tree and linear regression	–
ML	Machine learning	–
Nu	Nusselt number	–
PCM	Phase change material	–
POA	Plane-of-array irradiance	W/m^2
PTC	Parabolic trough collector	–
PTSC	Parabolic trough solar collector	–
R^2	Coefficient of determination	–
RAE	Relative absolute error	%
RH	Relative humidity	%
RMSE	Root mean square error	°C
SDR	Standard deviation reduction	–
SR	Solar radiation	W/m^2
SVM/SVR	Support vector machine / support vector regression	–
T_a	Ambient temperature / dead-state temperature	°C or K
T_i	Inlet temperature	°C or K
T_o	Outlet temperature	°C or K
$T_{\_outlet\_PTC}$	PTC outlet temperature	°C
T_{sun}	Apparent solar temperature	K
WS	Wind speed	m/s
A_s	Reflector/aperture surface area	m^2
cp	Specific heat capacity of air	J/kg·K
E_{nout}	Annual/net useful energy output	Wh/year
Ex_i	Exergy input	W
Ex_o	Exergy output	W
$\dot{E}x_{des}$	Exergy destruction	W
f	Friction factor	–
h_i	Inlet specific enthalpy	J/kg
h_o	Outlet specific enthalpy	J/kg
n	Annual sunshine duration	h/year
Q_u	Useful heat gain	W
U_R	Total uncertainty of calculated parameter	–
U_{xi}	Uncertainty of measured variable	–
zCO_2	Unit carbon price	USD/ton CO_2
ZCO_2	Carbon credit value	USD/year
Δh	Enthalpy change	J/kg
η_{en}	Energy efficiency	%
η_{ex}	Exergy efficiency / second-law efficiency	%
θ	Incidence angle	degree
φ_{CO_2}	Avoided CO_2 emission	ton/year
ρ	Density	kg/m^3
μ	Dynamic viscosity	Pa·s

of the selective coating. These thermal challenges reduce the overall efficiency and durability of the system [5].

To overcome these challenges, various techniques, including passive, active, and hybrid methods, have been developed and analyzed to improve the thermal performance of PTC [6]. Passive techniques include geometric modifications or the use of advanced fluids (nanofluids) to increase the heat transfer area, promote turbulence, or delay boundary layer formation [7]. Literature on topics similar to this research is summarized below by content.

The literature reports that various combinations of nanofluids and hybrid nanofluids are used to enhance the thermal performance of PTC systems. These studies have demonstrated that heat transfer and collector efficiency can be improved by enhancing the thermophysical properties of the working fluid. However, the use of nanofluids requires further evaluation regarding cost, stability, pumping power, and long-term operational reliability [8–10]. In this study, air was selected as the working fluid, and helical and trapezoidal turbulators were installed in the absorber tube to enhance heat transfer. Thus, performance improvement was sought through a passive geometric method that increases mixing by disrupting the internal flow structure, rather than by altering the fluid properties.

1.1. Receiver tube improvements

Placing internal elements (internal parts, internals) within the receiver tube is an effective passive approach to reducing heat loss and improving heat transfer performance. In this context, numerous studies in the literature address this issue. Kumar and colleagues [11] investigated the performance of a PTC with porous disks and fins and found that heat transfer increased by approximately 13%. Mwesigye and colleagues [12] reported that twisted-tape inserts separated from the wall could increase heat transfer by up to 169%. Mohammed and colleagues [13] performed a Computational Fluid Dynamics (CFD) analysis to improve PTC performance using conical turbulators and demonstrated a 233.4% increase in thermal performance for a nanofluid composed of Ag nanoparticles, SWCNT, and Syltherm oil. Similarly, it has been shown that corrugated turbulators inside the pump can increase PTC performance by up to 150.4%.

However, the use of such complex or sophisticated internal elements often significantly increases operational complexity and pump power demand. Ghadirijafarbeigloo and colleagues [14] found that slotted twisted strip supports increased the Nusselt number (*Nu*) by up to 250%, but also increased the friction factor (f) by a factor of 4. In particular, Liu and colleagues [15] reported more adverse effects, suggesting that conical inserts increase Nu by a factor of 2 while increasing the friction factor by a factor of 17. These findings show that simple-geometry, non-porous internal elements are still preferred in engineering applications because complex internal elements incur significant operating costs due to high friction factors.

In this context, investigating simple vane attachments offers a potential solution to these challenges. A study by Liu et al. [16] analyzed the effects of increasing the number of internal vanes on the performance of PTSCs based on Cu-Therminol®VP-1 nanofluid. Using five vanes resulted in a 64.8% increase in *Nu*, a 36.1% increase in f, and a 4.0% increase in thermal efficiency (for inlet temperature Tin = 400 K, *Re* = 105). Additionally, *Al*-Aloosi et al. [17] focused on a new design with added vanes at increased heights. For the sixth model (six fins), the maximum Thermal Performance Factor (TPF) was 1.4 at *Re* = 4000. Round-section fins provided a higher TPF (1.4) compared to elliptical (%1.31) and square (%1.26) sections.

1.2. Computational modeling integration

Analyzing the complex thermal and hydraulic behavior of PTC systems is limited by traditional analytical solutions [18]. Therefore, Computational Fluid Dynamics (CFD) is widely used to deeply

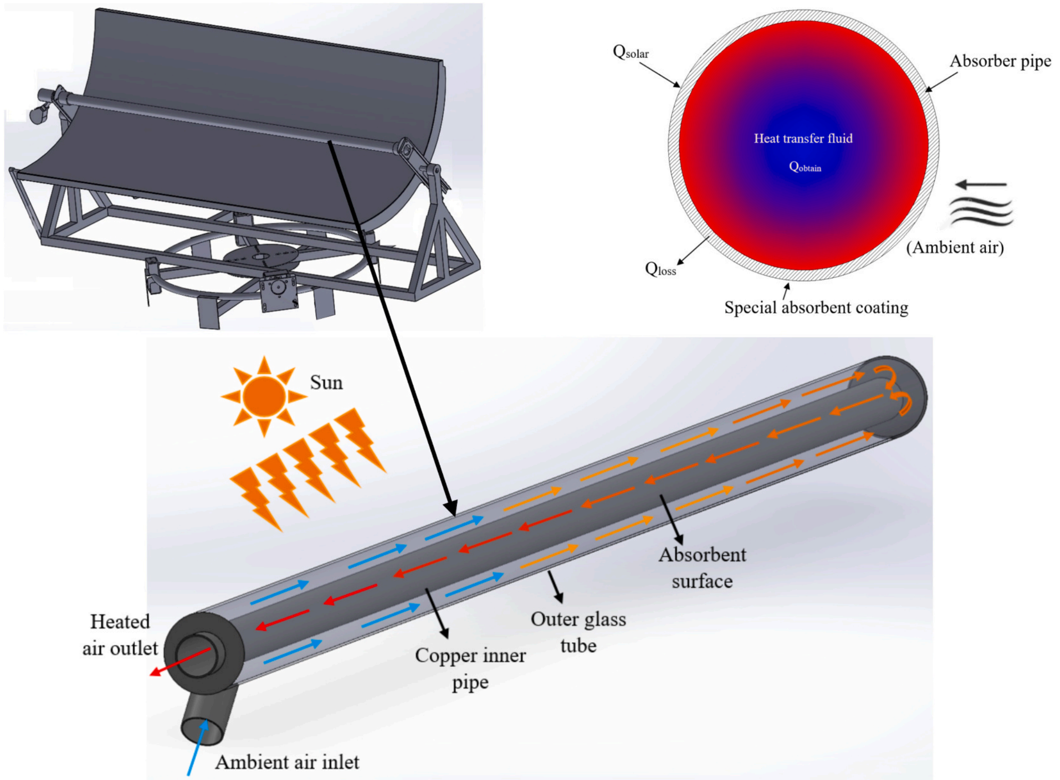

Fig. 1. The parabolic trough collector and geometry.

understand heat transfer mechanisms and evaluate new designs [19]. CFD simulates multiple physical phenomena, such as radiative heat transfer between the parabolic drain envelope and the absorber tube, conductive heat transfer at the tube wall, and fluid flow within the HTF [16]. CFD simulations are typically performed by solving the Navier-Stokes equations under the assumption of turbulent, incompressible flow [16]. Byiringiro et al. [19] and *Al*-Aloosi et al. [20] used the Realizable $k - \epsilon$ turbulence model because it better predicts the characteristics of separated flows. Amal et al. [18] evaluated the thermal performance of the receiver element by developing mathematical correlations for temperature-dependent thermophysical properties; this approach increased thermal performance by 1.4%.

Although CFD provides accurate results, it can be computationally costly and time-consuming when evaluating a wide range of design parameters, especially for receiver tube modifications (such as curved lobed tubes). Rabienataj Darzi and colleagues [21] highlighted this challenge and emphasized the importance of hybrid approaches combining CFD with artificial intelligence (AI) and machine learning (ML) techniques.

1.3. Artificial intelligence-based optimization and prediction

Machine learning methods such as Artificial Neural Networks (ANN), Support Vector Machines (SVM/SVR), and Decision Trees (DT) are widely used to predict the outlet temperature and efficiency of PTC systems with reduced computational cost [22]. Alhamayani [23] reported that ANN outperformed DT and SVM models, achieving an R^2 of 99.99%, while Kottala et al. [24] showed that Gaussian Process Regression (GPR) provided high accuracy ($R^2 = 0.9977$) in predicting the thermal efficiency of a PCM-based receiver tube.

In addition to prediction, AI-based approaches are increasingly applied to design optimization and decision-making. Rabienataj Darzi et al. [21] combined ANN and Genetic Algorithm (GA) with CFD data to optimize receiver tube geometry, achieving higher performance than DOE-based methods. Similarly, Hu et al. [25] demonstrated that CFD-trained SVR and ANN models outperform linear regression. For heat transfer fluid selection, Yılmaz et al. [26] integrated CFD-supported AHP and VIKOR methods and identified water as the most suitable HTF.

In recent years, efforts to improve the performance of PTC systems have focused on using different working fluids, improving receiver tube geometry and internal components, conducting CFD-supported analyses, and developing data-driven prediction approaches. For example, recent studies have compared water and various thermal oils as working fluids in PTC systems and demonstrated that fluid selection has significant effects on collector performance [27]. Furthermore, recent thermal system research highlights the importance of CFD-based and geometry-focused analyses in understanding complex flow and heat transfer mechanisms [28]. However, a significant portion of current studies focuses on only one of the following: experimental testing, CFD analysis, or data-driven prediction approaches. In this study, the effects of helical and trapezoidal turbulators in an air-based PTC system were evaluated using experimental measurements, validated three-dimensional CFD analyses, and interpretable artificial intelligence models. This approach not only explains the physical effects of the turbulators on the flow and temperature fields but also enables rapid, interpretable prediction of the outlet temperature based on environmental parameters.

The primary objective of this study is to improve the thermal and exergetic performance of PTC under real environmental conditions and to explain the underlying physical mechanisms while enabling rapid performance prediction. For this purpose, an air-based double-pass PTC was designed, manufactured, and experimentally tested, and its energy–exergy performance and environmental indicators were evaluated. The experimental results were validated using a three-dimensional CFD model, and the heat transfer enhancement effects of two turbulator geometries (trapezoidal and helical) installed in the receiver pipe were comparatively analyzed. In addition, interpretable artificial intelligence methods (M5P decision tree and Elastic.Net) were employed to predict the PTC outlet temperature from environmental parameters, providing

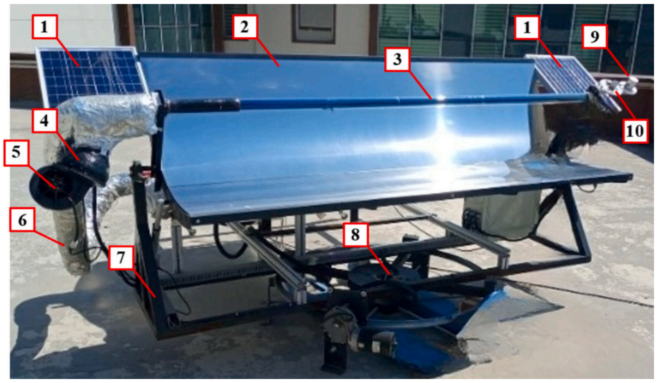

Fig. 2. System components of the PTC.

Table 1
System components and features.

System Component	Specifications	Brand / Type	Accuracy / Tolerance
Centrifugal Fan	Air flow rate: 1050–1200 m^3/h; Static pressure: 40–70 Pa; Power consumption: 30–40 W; Supply: 230 V / 50 Hz	Fanexfan/Turkiye	Air flow: ±5%, Power: ±3%
Polycrystalline PV Panel (55 W)	Rated power: 50–60 W; Vmp: 17–19 V; Imp: 2.8–3.3 A; Module efficiency: 14–16%	Victron Energy / Renogy / CW Enerji	Power: ±3%, Voltage: ±2%
Parabolic Reflector	Length: 2 m; Aperture width: 1.2 m; Focal length: 0.27 m; Rim angle: 83.6°; Aperture area: 3.6 m^2	Custom-made (Aluminum reflective surface)	Geometric tolerance: ±1 mm
Receiver Tube	Outer diameter: 0.057 m; Inner diameter: 0.028 m; Length: 2 m; Receiver area: 0.32 m^2; Geometric concentration ratio: 6.7	Custom-made (Copper absorber tube, black matte coating)	Diameter tolerance: ±0.1 mm

The experimental system is designed as an integrated structure consisting of four main components. The airflow in the receiver pipe is provided by a low-power centrifugal fan operating at 1050–1200 m^3/h, and the fan's energy requirement is met by a 55 W PV panel. Solar radiation is concentrated by a parabolic reflector and directed to the black matte-coated copper receiver pipe, where heat is transferred to the working fluid. The reliability of the experimental results was ensured by maintaining measurement accuracies and geometric tolerances under control. This setup allows for the thermal performance of the PTC, CFD analyses, and second law-based evaluations to be performed.

accurate predictions and physically interpretable equations. Overall, the study offers an integrated experimental–numerical–AI framework for performance enhancement and rapid, interpretable prediction in PTC systems.

The innovative aspect of this study is that the thermal effects of helical and trapezoidal turbulators within a PTC absorber tube are evaluated not only numerically but also through experimental validation and an AI-supported prediction approach. First, the turbulator geometries were compared using three-dimensional CFD analyses; subsequently, a helical turbulator was manufactured and installed in the experimental system due to its higher outlet-temperature enhancement under the investigated CFD conditions. The experimental data obtained were used both to validate the numerical model and to predict the outlet temperature using interpretable artificial intelligence models such as M5P and Elastic.Net. In this regard, the study presents an integrated approach to evaluating the use of internal turbulators in PTC systems, covering heat transfer, energy output, environmental impact, and rapid performance prediction. The thermal processes addressed in this study mainly involve forced convection inside the absorber tube, thermal boundary-layer disruption, enhanced fluid mixing, and outlet-air heating under concentrated solar loading. These processes are directly relevant to practical air-based thermal applications such as solar drying, process-air heating, and medium-temperature heat-recovery systems, where improved outlet temperature and thermal efficiency are essential for system effectiveness.

2. Materials and methods

In this study, an air-based double-pass PTC was designed and experimentally investigated under Tokat conditions. The thermal and environmental performance of the collector was evaluated using experimental data, and the numerical model was validated through CFD analyses. To increase efficiency, two different turbulator geometries were designed, and the most suitable structure was determined using CFD analyses and applied to the experimental system. Numerical models were created in SOLIDWORKS 2018, and analyses were performed using ANSYS FLUENT 18.1. Additionally, an artificial intelligence-based model was developed to capture the environmental parameters that affect the outlet temperature. This section presents the experimental setup, calculation procedure, validation strategy, CFD assumptions, and AI workflow forming the basis of the reported findings.

2.1. Experimental setup and procedure

This study focuses on improving the thermal behavior and efficiency of PTC in Tokat Province, Türkiye. The test system, consisting of the PTC and a drying chamber, was operated from September 15 to 17, 2023, with stable air temperature, humidity, wind speed, and solar radiation. Each morning, researchers set the environmental parameters and assembled the system. Tests were run, and data were collected and recorded under controlled conditions. Results were logged after each session, and the process was repeated daily to ensure consistency; the data from all three days were later averaged. Fig. 1 shows the setup: a double-pass vacuum-tube solar collector that focuses solar energy and turns it into heat. A 27 mm copper pipe at the collector's center is in contact with the airflow to boost heat transfer. A fan maintains airflow, sending hot air to a greenhouse-type drying chamber via pipes.

In this study, the greenhouse-type drying chamber was used only as the downstream application unit where the heated air leaving the PTC was directed. The thermal evaluation and performance comparison mainly focus on the PTC receiver tube, outlet air temperature, and the effects of the internal turbulators rather than on the drying chamber performance. This study did not include testing of any drying products. Additionally, drying kinetics, product moisture removal, drying rate, and temperature–humidity distribution within the drying chamber were not addressed.

In Fig. 2, the system shown was manufactured after the design phase, and various experiments were conducted. The experiments were repeated over three days, and the data were averaged. The experiments lasted 420 min with 5-min measurement intervals. In the experimental studies, data were collected using sensors placed in various areas of the system.

As shown in Fig. 2, the working fluid (ambient air) is drawn into the system by a fan (5) and first passes through the double-pass absorber pipe (3). The air flowing inside the absorber is heated by solar radiation reflected from the parabolic concentrator and is then delivered through the insulated pipe section (6). During the experiments, data were recorded using radiation sensors (9) placed outside the system and temperature sensors (5–10) located at various positions. Air was supplied at a constant velocity of 2 m/s through a copper absorber pipe with an outer diameter of 27 mm, a wall thickness of 1 mm, and a total length of 2000 mm, coated with black matte paint (Fig. 2). The system components and detailed specifications of the PTC are summarized in

Table 2
Measurement device specifications and accuracies.

Sensor	Measurement Range.	Brand	Uncertainty	Unit
Air velocity transmitter	0–20	HK Instruments	±0.2 of value	m/s
PT 100	50 °C–205 °C	Baumer	±0.3	°C
Pyranometer	0–2000	Kipp & Zonen	±0.2	W/m^2
Thermohygrometer	40 °C–125 °C	DFROBOT	±(3% + 0.3)	°C

Table 1.

3. Measurement equipment and data recording

Table 2 presents the type, measurement range, and accuracy of the sensors used in the experiments. The low error rates of the sensors measuring environmental parameters demonstrate the reliability of the experimental data. This measurement accuracy provides a robust data infrastructure for thermodynamic analyses and artificial intelligence-based modeling.

3.1. Calculation Procedure

3.1.1. Conversion of radiation data and separation model

Efficiency calculations for PTC are typically referenced to Direct Normal Irradiance (DNI), as the concentrated useful gain depends on the beam component of solar radiation. In this study, solar irradiance was measured as global radiation on the collector plane (SR_global, Plane-of-Array) using a pyranometer aligned with the collector aperture plane. To derive DNI values suitable for concentrating-system analysis, the measured plane-of-array (POA) irradiance was converted to horizontal global irradiance (GHI) through a standard transposition method based on solar geometry and collector orientation. The GHI values were subsequently decomposed using the Erbs et al. (1982) model to estimate the diffuse fraction, and DNI was calculated from the beam-horizontal component using the solar zenith angle [29,30]. The Erbs decomposition model is an empirical method for estimating the diffuse and direct components of measured solar radiation. While widely used for its simplicity and practicality, the resulting DNI values may be affected by sky conditions, solar geometry, and local atmospheric variations. As a result, DNI values were used as consistent comparative input data across all configurations, rather than as absolute indicators of optical performance. This limitation was taken into account when interpreting the thermal and exergetic results of the PTC system.

3.1.2. Energy efficiency calculation

In PTC, useful energy is expressed in Eq. 1 based on the inlet (Ti) and outlet (To) temperatures of the fluid [31].

$$Q_u = \dot{m}c_p(T_o - T_i) \tag{1}$$

In Eq. 1, the mass flow rate of the fluid passing through the PTC is (kg/s), and cp is the specific heat of air (J/kg · K). According to the first law of thermodynamics, the energy efficiency of the PTC is expressed using Eq. 2 [32]. The energy efficiency of the system is defined as the ratio of the useful energy absorbed to the power generated by solar radiation. In Eq. 2, η_{en} is the energy efficiency, DNI is direct normal solar radiation incident on the PTC surface (W/m^2), and A_s is the surface area of the reflector in the PTC (m^2).

$$\eta_{en} = \frac{\dot{m}c_p(T_o - T_i)}{DNI.A_s} \tag{2}$$

The solar radiation value in this study was taken as DNI (Direct Normal Irradiance). The DNI term in Eq. (2) represents the useful energy incident on the collector aperture of a PTC, a concentrating system. Since the system is a two-axis solar tracking system, the angle of incidence θ between the collector aperture plane and the solar rays was assumed to be approximately zero at the time of measurement, and therefore, the projection of the radiation onto the aperture plane was expressed directly through DNI, assuming cos(θ) ≈ 1. DNI values were determined based on radiation data recorded in the field with a pyranometer and solar geometry; this obtained DNI was used as a consistent reference input in efficiency and exergy analyses in Eq. (2). This approach enhances the comparability of results by allowing the energy input to be defined directly in terms of its components, particularly in experimental studies comparing the thermal and exergetic performance of different receiver tube internal geometries (turbulator/non-turbulator) under the same optical conditions [33].

3.1.3. Exergy analysis

Exergy equations can be derived based on certain assumptions [34]. Exergy balance ratios can be expressed by neglecting changes in kinetic and potential energy. Under these conditions, Eqs. 3 and 4 express the amount of exergy destruction [35].

$$\sum \dot{E}x_{des} = \sum \dot{E}x_i - \sum \dot{E}x_o \tag{3}$$

$$\dot{E}x_{des} = \left(1 - \frac{T_a}{T_{sun}}\right).DNI.A_s - \dot{m}\left[(\Delta h) - T_a\left(ln\frac{Ta}{T_i}\right)\right] \tag{4}$$

$\dot{E}x_{des}$ represents the amount of exergy destruction (W), indicating irreversibility. For exergy calculations, the relevant parameters include the air temperature Ta (K) (dead-state temperature) and the solar surface temperature Tsun (K), both assumed to be 4350 K [35]. Subsequently, the enthalpy change Δh (J/kg) of air passing through the PTC's absorber pipe is given by Eq. 5.

$$\Delta h = h_o - h_i \tag{5}$$

The second law efficiency, also known as exergy efficiency, is determined using Eq. 6 [35], providing a robust framework for analyzing system performance.

$$\eta_{ex} = \frac{Ex_o}{Ex_i} = \frac{\dot{m}\left[(\Delta h) - T_a\left(ln\frac{T_a}{T_i}\right)\right]}{\left(1 - \frac{T_a}{T_{sun}}\right).DNI.A_s} \tag{6}$$

3.1.4. Energy-Based Environmental Impact Analysis

This study assessed the environmental performance of PTC by integrating exergy-based indicators with a CO_2-focused approach. The environmental impact analysis used a carbon intensity of 0.408 kg CO_2/kWh, as reported in a recent scenario study for the Turkish electricity sector [36]. Carbon intensity may vary with grid structure, generation mix, and transition scenarios. As a result, avoided CO_2 emissions and carbon credit values should be evaluated according to the chosen emission factor. Using this factor, the yearly amount of CO_2 avoided by the system is evaluated through Eq. (7) [37]:

$$\varphi CO_2 = \frac{E_{nout}\ x\ n\ x\ EF_{CO2}}{1000} \tag{7}$$

In Eq. (7), φCO_2 denotes the environmental output expressed in tons of CO_2. The term *Enout* represents the net useful power delivered by the collector (kW), whereas n corresponds to the annual sunshine duration of the experimental site (h/year) [38]. The annual sunshine duration (n) was estimated from the long-term official meteorological statistics for Tokat province. According to the Turkish State Meteorological Service, the n value for Tokat is 5.9 h/day, corresponding to approximately 2154 h/year, and this value was used to estimate the yearly environmental benefits [39]. The EF_{CO2} is the grid emission factor in kgCO_2/kWh. In this study, EF_{CO2} was taken as 0.408 kgCO_2/kWh. The divisor 1000 is used to convert kgCO_2 to tonCO_2.

The annual sunshine duration used in this study should not be interpreted as the sunshine duration of the three experimental days in

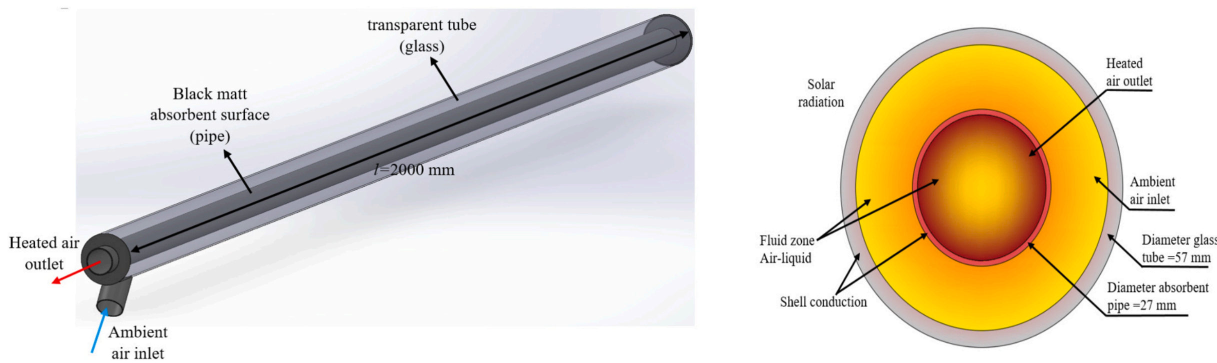

Fig. 3. 3D CFD Model domain.

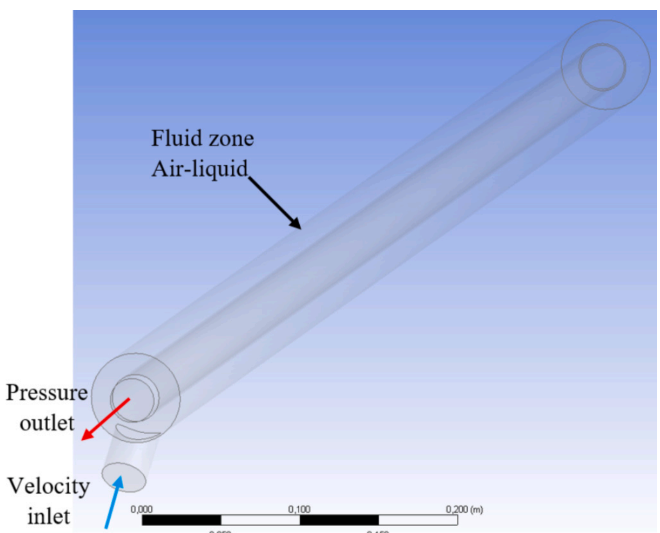

Fig. 4. Flow volume.

September. The experimental data were used to obtain the representative useful energy output of the PTC under measured operating conditions. In contrast, the annual sunshine duration was employed only to annualize this measured performance under the long-term climatic conditions of Tokat. Since the experimental days represent a short seasonal period with relatively high sunshine duration, using only the measured daily sunshine hours of these days for annual extrapolation could overrepresent September conditions. Therefore, the long-term annual average sunshine duration of Tokat, 5.9 h/day corresponding to approximately 2154 h/year, was used to provide a more representative and conservative yearly estimate of useful energy output and CO_2 mitigation potential.

To express the environmental benefit in monetary terms, a carbon-credit formulation was employed. As stated in Eq. (8), the carbon-credit value is obtained by multiplying the avoided CO_2 by the unit carbon price ZCO_2. In this study, the global carbon price was assumed to be 14.5 USD per ton of CO_2 [40]:

$$ZCO_2 = zCO_2 \; x \; \varphi CO_2 \tag{8}$$

3.1.5. Uncertainty Analysis

The uncertainties associated with calculated parameters derived from measured quantities, including energy efficiency, exergy efficiency, and other performance indicators, were determined using the Holman uncertainty propagation method [41]. The total uncertainty of any calculated magnitude defined as R = f(x1, x2, …., xn) is given by the following equation:

$$\hat{y}_i = U_R = \sqrt{\left(\frac{\partial R}{\partial x_1}U_{x_1}\right)^2 + \left(\frac{\partial R}{\partial x_2}U_{x_2}\right)^2 + \ldots.. + \left(\frac{\partial R}{\partial x_n}U_{x_n}\right)^2} \tag{9}$$

Uncertainty values for solar radiation, inlet and outlet air temperature, air velocity, and ambient temperature, which were directly measured in the experimental studies, are presented in Table 2. In contrast, useful energy gain, energy efficiency, exergy loss, exergy efficiency, and environmental performance indicators are calculated parameters derived from these measured variables. The error-propagation method was applied to assess the impact of measurement uncertainties on these calculated parameters. Combined uncertainty calculations followed the Holman approach. For any quantity R = f(x1, x2, …, xn) dependent on independently measured variables, total uncertainty was determined using the partial derivative-based error propagation method. In this approach, the uncertainty contribution of each measured variable was evaluated separately and the combined uncertainty was calculated as the square root of the sum of the squares of individual uncertainties. During the stable, high-radiation period analyzed, a representative DNI model uncertainty was included in the uncertainty propagation for ηen, Exi, and ηex, highlighting that these parameters were affected by the estimated DNI from the Erbs decomposition model rather than direct measurement. This model-related uncertainty varies with sky conditions, solar geometry, and temporal resolution.

3.2. Error Calculation for Validation

In this study, temperature and humidity measurements from the experimental vacuum tube dryer system, along with solar radiation and power consumption data, were used to evaluate the accuracy of CFD analyses. The CFD validation was performed using the experimentally measured outlet-temperature data obtained from the present air-based PTC system. Quantitative assessment of the agreement between experimental and CFD outputs was performed using the mean absolute error (MAE) and root mean square error (RMSE). These statistical metrics quantify the mean and overall deviations between measured and predicted values, respectively. The mathematical formulations for these metrics are provided in Eqs. 10 and 11. In these equations, y denotes the predicted value, x the actual value, and n the number of samples in the dataset.

$$MAE = \frac{|y_1 - x_1| + \ldots + |y_n - x_n|}{n} \tag{10}$$

$$RMSE = \sqrt{\frac{1}{n}\sum_{i=1}^{n}(y_i - x_i)^2} \tag{11}$$

3.3. Computational Fluid Dynamics Model (CFD)

In the CFD section, three-dimensional flow and heat transfer in the

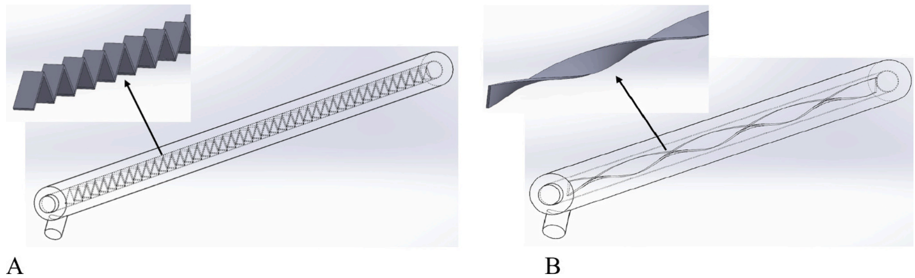

Fig. 5. The arrangement of turbulators inside the absorber tube.

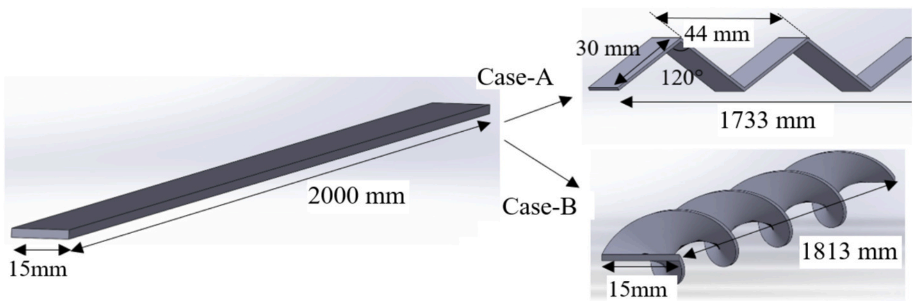

Fig. 6. Trapezoidal (Case A) and helical (Case B) turbulators.

Table 3
Mesh statistics.

Case	Element Number	Max. Mesh dim. [mm]	Grow rate	Max.-Ave Skewness	Number of layer used in boundary layer
Type-1	1,586,622	3	1.2	0.684–0.23	8
Type-2	670,940	4	1.2	0.812–0.23	8
Type-3	347,184	5	1.2	0.916–0.24	8

PTC were analyzed in two stages. First, numerical results aligned with experimental data. Next, thermal behavior for helical and trapezoidal turbulators was evaluated. Fig. 3 shows the PTC geometry and thermal principles, including a cross-section of a double-pass receiver pipe. The model only included the receiver pipe: a 27 mm copper pipe with a black matte coating ($\varepsilon = 0.9$) inside a 57 mm glass tube. Air was used as the working fluid, with a set inlet velocity and monitored outlet pressure. Fig. 4 presents the resulting flow conditions.

The study examines two passive enhancement strategies: (i) trapezoidal turbulators and (ii) helical turbulators. Fig. 5 shows the types of turbulators used and how they are positioned inside the suction

Table 4
Fluid and solid thermal properties used in numerical analysis.

Material	Density kg/m^3	Specific heat J/kgK	Thermal conductivity W/mK
Aluminum	2719	871	202.4
Air	1.225	1006	0.0242

Table 5
Data set parameters used in artificial intelligence models.

Input Parameters		
Parameter	Symbol	Min/Max
Solar Radiation (W/m^2)	SR	180/969
Ambient Temperature (°C)	T_a	28.5/36.92
Relative Humidity (%)	RH	17.5/22.6
Wind Speed (m/s)	WS	0.6/3.8
Output Parameter		
Parameter	Symbol	Min/Max
PTC Outlet Temperature (°C)	T_outlet_PTC	40.06/152.756

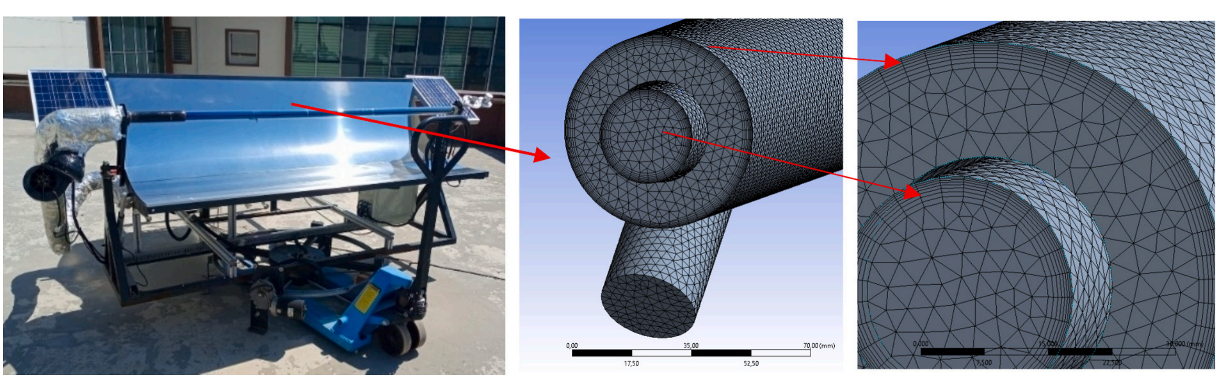

Fig. 7. 3D MESH Model domain.

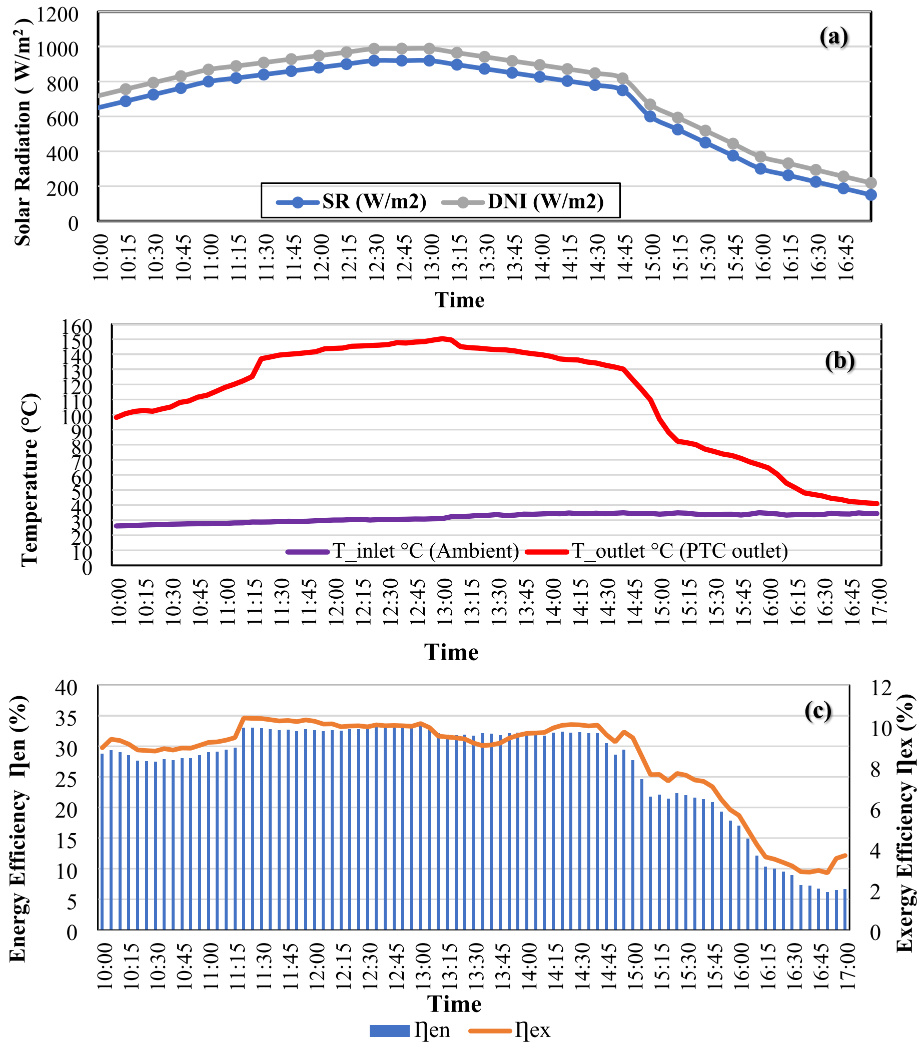

Fig. 8. Experimental performance results of the reference PTC system: (a) variation of solar radiation with time, (b) variation of inlet and outlet air temperatures with time, and (c) variation of energy and exergy efficiencies with time.

Table 6
Uncertainty values of the calculated performance parameters.

Calculated parameter	Main variables used in calculation	Unit	Uncertainty value
Useful energy gain, Q_u	$\dot{m}$, cp, T_o, T_i	W	±2.6%
Energy efficiency, η_{en}	Q_u, DNI, A_s	%	±5.8%
Exergy input, Ex_i	DNI, A_s, T_a, T_{sun}	W	±5.7%
Exergy output, Ex_o	$\dot{m}$, cp, T_o, T_i	W	±3.2%
Exergy efficiency, η_{ex}	Exi, Ex_o	%	±6.0%

Table 7
Annualized energy and CO_2 mitigation indicators based on long-term sunshine duration.

Parameter	PTC without Turbulator	PTC with Helical Turbulator	PTC with Trapezoidal Turbulator
E_{nout} (Wh/year)	546,912	694,580	661,760
$Ø_{CO2}$ (ton/year)	0.223	0.283	0.270
Z_{CO2} ($/year)	3.24	4.10	3.91

pipe.

The trapezoidal and helical section turbulators installed in the suction pipe are made of aluminum, with a thickness of 2 mm, a width of 12 mm, and a length of 2000 mm. Their geometries are shown in Fig. 6. Although both types have the same surface area, their developed lengths differ due to their shapes: the trapezoidal section is 1733 mm long, and the helical section is 1820 mm long. The trapezoidal design has a triangular shape with a 30 mm × 30 mm base and a 120° peak angle, while the helical design is formed by rotating the strip through two full turns.

The numerical mesh employed a multi-domain structure, and mesh sensitivity was evaluated using three different cell sizes (3, 6, and 9 mm). The mesh was locally refined near the walls to improve near-wall resolution, with $y+$ values maintained below approximately one. Mesh quality was assessed using skewness, and the corresponding results are presented in Table 3, while a detailed mesh view is shown in Fig. 7. To ensure reliability, three mesh models were generated and their results were compared with experimental data through a mesh independence test.

The Type-1 mesh for the standard PTC includes 1,586,622 elements, with a maximum curvature of 0.684 and an average skew of 0.24. For the absorber pipe with turbulators, the trapezoidal and helical

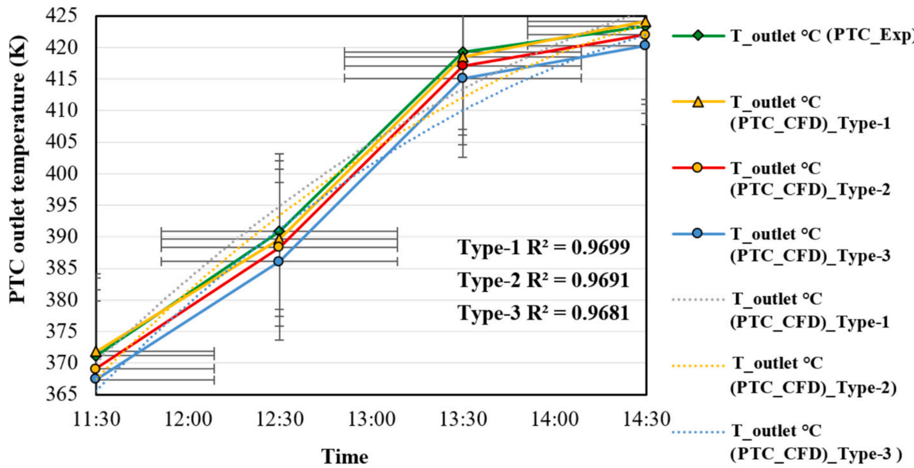

Fig. 9. Mesh independence test with CFD–experimental outlet-temperature comparison.

Table 8
Mesh characteristics and validation error metrics for the grid independence analysis.

Mesh type	Average y^+	Maximum y^+	MAE	RMSE
Type-1	0.62	0.98	0.85	0.86
Type-2	1.18	1.74	2.04	2.07
Type-3	2.35	3.12	3.96	3.99

geometries contain 1,573,892 and 1,563,950 elements, respectively. The presence of turbulators increases local curvature and skewness, with maximum skew values of 0.815 (trapezoidal) and 0.692 (helical), while average skew values remain similar. The thermal properties of the materials used in the numerical analysis are listed in Table 4.

In the present CFD model, the thermophysical properties of air and solid materials were assumed constant for numerical simplicity. However, since the operating temperature of the receiver tube reaches approximately 140–150 °C, temperature-dependent variations in properties, especially air density, viscosity, and specific heat, may influence local heat transfer and pressure-drop predictions. Therefore, this assumption should be considered as a limitation of the present model. Recent review studies have also emphasized the importance of accurate thermophysical property characterization in receiver-tube analyses of parabolic trough collectors [42].

In order to maximize the physical realism and numerical accuracy of the 3D CFD simulations conducted in this study, the solar radiation inputs defined on the receiver tube surface were directly derived from field measurements. Throughout the analyses, instead of relying on hypothetical outputs from standard theoretical radiation models (such as Rosseland), real-time data recorded at 15-min intervals via a pyranometer were utilized. In this context, for each specific simulation hour (11:30, 12:30, 13:30, and 14:30), the measured global solar radiation values were decomposed into their Direct Normal Irradiance (DNI) components using the Erbs et al. decomposition model. These derived experimental DNI values were then applied directly to the outer surface of the absorber tube as instantaneous heat flux boundary conditions. This approach ensured that atmospheric uncertainties and transient radiation fluctuations were precisely reflected in the numerical model, allowing the thermal response of the collector to be simulated in full synchronization with the local climatic conditions of Tokat province. No additional radiation model such as DO, P1, or Rosseland was activated in the present CFD study; therefore, detailed surface-to-surface radiative exchange between the absorber tube and glass envelope was not explicitly resolved and should be considered as a model limitation [43].

The CFD model was developed to simulate three-dimensional turbulent forced-convection heat transfer inside the absorber tube of the parabolic trough collector under experimentally defined solar loading conditions [6]. The numerical formulation was based on the conservation equations of mass, momentum, and energy for the air domain inside the receiver tube [6].

In the present study, the flow was assumed steady, three-dimensional, and turbulent, while air was treated as an incompressible Newtonian fluid with constant thermophysical properties. The absorber wall was subjected to hourly solar heat-flux boundary conditions derived from experimental measurements. No separate radiation model was activated; instead, measured solar radiation values for selected hours were directly imposed on the absorber surface as boundary conditions [6,44].

The main modeling hypothesis is that internal turbulators disturb the thermal boundary layer, enhance fluid mixing, and thereby improve convective heat transfer and outlet air temperature [1]. The turbulence field was modeled using the realizable k-epsilon model, which is widely used in internal-flow and solar collector simulations [1,45].

In the CFD analysis of the PTC, turbulent flow inside the absorber tube was modeled under forced convection conditions using the realizable k–ε turbulence model, which is widely adopted in similar studies [20,46,47]. Enhanced wall treatment was applied to improve near-wall resolution, and the governing equations were solved using the finite-volume method [48]. Pressure–velocity coupling was handled with the SIMPLEC algorithm, and convergence criteria of 10^{-6} for flow variables and 10^{-8} for energy were satisfied in all simulations [49]. The governing equations used in the CFD analysis are provided in the ***Supplementary Material*** to improve the clarity and conciseness of the main text.

3.3.1. Initial and boundary conditions

In the CFD model, a uniform velocity profile was prescribed at the absorber tube inlet to represent the fan-driven airflow supplied to the experimental system. The flow was considered as developing turbulent flow from the inlet region, and the effects of the internal turbulators were evaluated under the same inlet and outlet boundary conditions for all configurations. Since the main objective was to compare the relative thermal and flow-field effects of the helical and trapezoidal inserts, the inlet condition was kept identical in all simulations. This approach allowed the influence of turbulator geometry on flow mixing, boundary-layer disruption, and outlet temperature to be assessed consistently.

In the CFD calculations, the relevant boundary and initial conditions have been combined with the fundamental equations mentioned above to simulate flow and heat transfer in all conditions of the absorber pipe. These conditions are listed below [20].

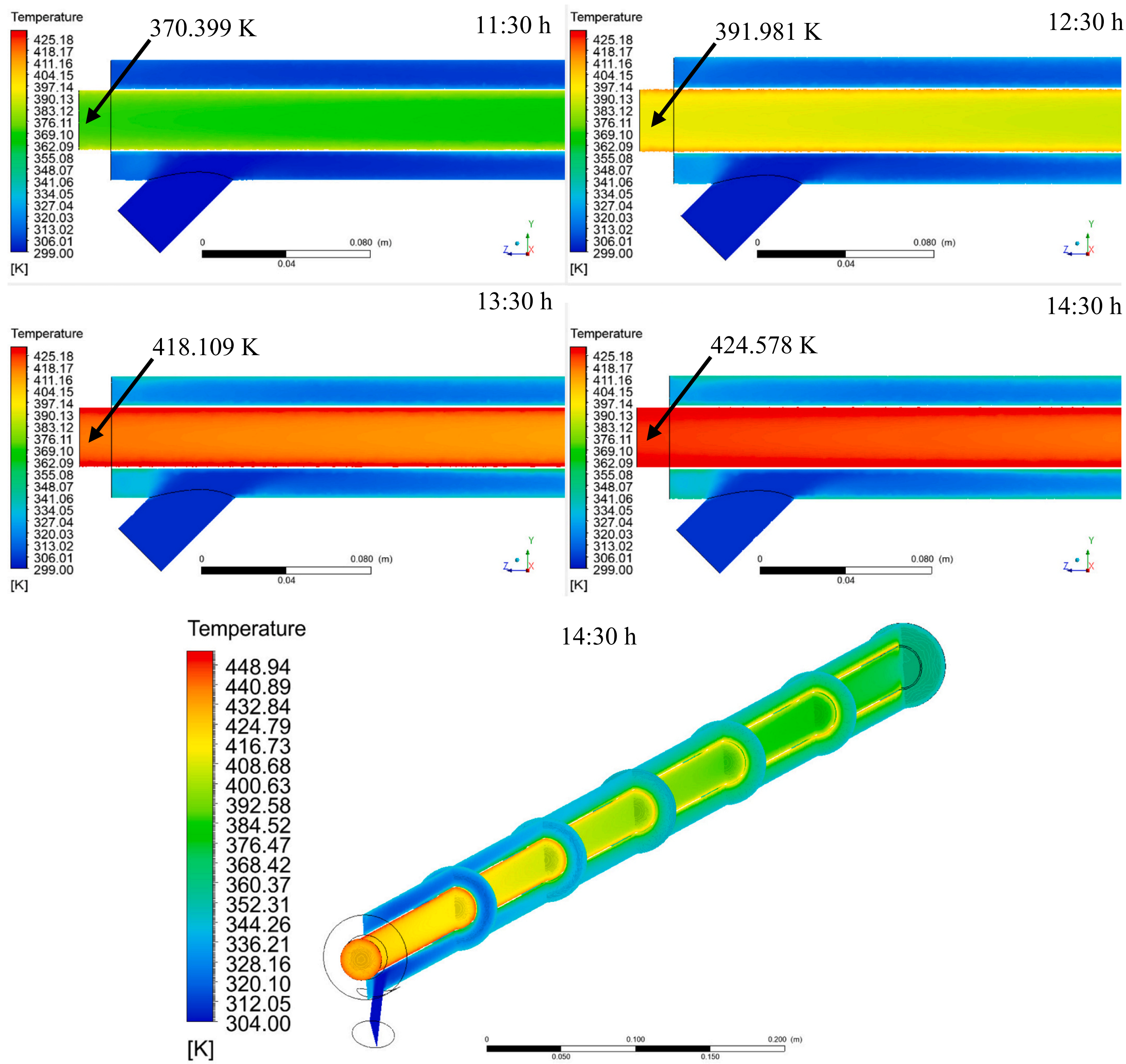

Fig. 10. Temperature distribution contours of CFD analyses.

- The airflow was modeled as three-dimensional, steady, and turbulent.
- A constant inlet temperature and a uniform inlet velocity profile were prescribed at the absorber tube inlet.
- The inlet turbulence conditions were defined using a turbulence viscosity ratio of 10% and a turbulence intensity of 5%.
- Air was treated as an ideal gas outside the absorber tube.
- No-slip boundary conditions were applied to all solid surfaces, including the absorber tube and turbulators.
- Time-dependent solar heat-flux boundary conditions, derived from experimental radiation data, were imposed on the outer wall of the absorber tube.
- A pressure outlet boundary condition was specified at the outlet.

A uniform inlet velocity profile was used in all CFD cases to ensure a consistent comparison between the reference and turbulator configurations, and the absorber-tube length was considered sufficient for flow development before the outlet region.

3.4. Artificial intelligence procedure

In the present study, CFD and interpretable AI were employed for different but complementary purposes. CFD analyses were used to physically evaluate the effects of turbulator geometries on flow structure, temperature distribution, and convective heat transfer within the absorber tube, whereas AI models were developed to provide rapid, interpretable predictions of the PTC outlet temperature based on environmental parameters. Therefore, the AI framework was not intended to replace the CFD analysis, but to complement it with a data-driven prediction tool.

In this study, M5P and Elastic.Net algorithms were used to model the fluid temperature obtained using solar energy and PTC according to

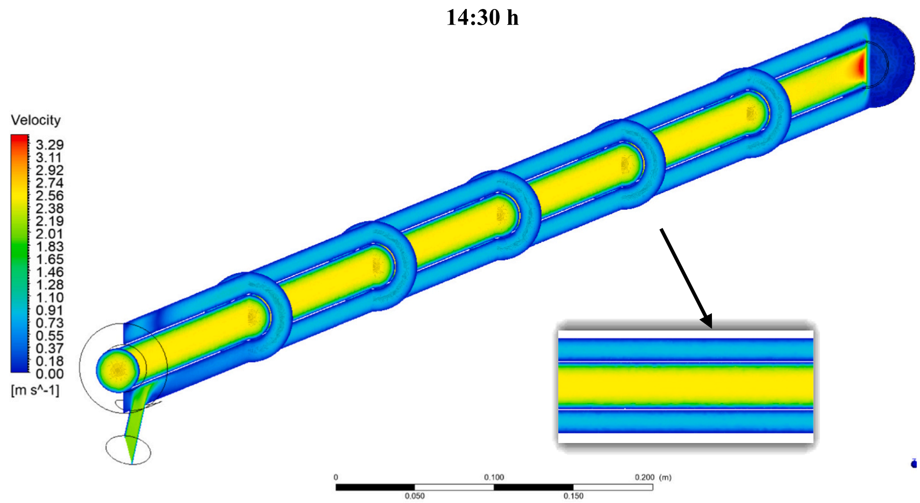

Fig. 11. Wind speed distribution contours from CFD analyses for 14:30 PM.

environmental parameters. The data set used in the artificial intelligence procedure is given in Table 5.

A total of 510 data samples were utilized in the artificial intelligence analysis. Prior to model development, the dataset was randomly reordered and partitioned into 70% for training and 30% for testing. This allocation ensured that the training set supported the development of the M5P and Elastic.Net models, while the testing set remained reserved for unbiased performance evaluation. During training, a 10-fold cross-validation procedure was implemented to enhance reliability. Since the dataset was collected over three consecutive experimental days, predictive performance should be interpreted within this specific temporal context, rather than as a broadly applicable seasonal model. The M5P model incorporated pruning, and the Elastic.Net model applied regularization; both strategies improved generalization performance. Predictive accuracy was assessed using R^2, MAE, and RMSE metrics calculated on the test dataset.

3.4.1. Decision Tree (M5P)

The M5P algorithm is a hybrid approach that combines decision tree learning with linear regression. Unlike conventional trees, linear regression models are constructed at the leaf nodes. The input space is recursively partitioned by maximizing variance reduction, and pruning and smoothing procedures are applied to improve generalization and reduce overfitting [50].

During tree construction, splits are selected based on standard deviation reduction (SDR):

$$SDR = sd(T) - \sum_{i=1}^{n} \frac{|T_i|}{|T|} \cdot sd(T_i) \tag{12}$$

At each terminal node, a multivariate linear regression model is fitted:

$$\widehat{y} = \beta_0 + \beta_1 x_1 + \beta_2 x_2 + \ldots + \beta_p x_p \tag{13}$$

The regression coefficients are estimated using ordinary least squares:

$$\widehat{\beta} = \left(X^T X\right)^{-1} X^T y \tag{14}$$

After tree induction, pruning is performed by comparing subtree and node prediction errors, and smoothing is applied to ensure continuity between parent and leaf predictions [51]:

$$\widehat{y}_{\text{smooth}} = \frac{n \cdot \widehat{y}_{\text{leaf}} + k \cdot \widehat{y}_{\text{parent}}}{n + k} \tag{15}$$

3.4.2. Elastic.net regression

Elastic.Net regression was used to model the relationship between PTC outlet temperature and multiple environmental and operating variables. By combining L1 (Lasso) and L2 (Ridge) regularization, Elastic.Net effectively addresses multicollinearity and overfitting in regression-based modeling [52].

The objective function minimizes the residual error while applying L1 and L2 penalties, enabling both variable selection and coefficient stabilization [53]. Unlike black-box models, Elastic.Net produces explicit linear equations that allow direct interpretation of input variable effects, which is particularly advantageous for thermal and energy systems [54]. Previous studies have demonstrated its successful application to various energy-related systems under different operating conditions [55]. Due to its ability to handle multicollinearity, prevent overfitting, and generate physically interpretable equations, Elastic.Net regression was selected as a reliable regression-based artificial intelligence method in this study to model PTC outlet temperature and support CFD analysis.

4. Results

In this section, CFD analyses validated by experimental measurements obtained from an air-based double-pass PTC system and the outputs of artificial intelligence-based prediction models are presented together to quantitatively evaluate the effects of turbulator geometries on thermal-exergetic performance and environmental indicators.

4.1. Experimental Results

This section presents the experimental performance results of the reference PTC system without a turbulator. The changes in solar radiation measured throughout the day and in the inlet–outlet air temperatures reflect the system's thermal response and serve as a reference for theoretical calculations and CFD analyses. Fig. 8a **and** Fig. 8b show that the radiation reaches maximum values at noon, with a parallel increase in the outlet temperature, while both values decrease in the afternoon. According to the theoretical results shown in Fig. 8c, the energy efficiency ranges from approximately 33–35% during midday hours, while the exergy efficiency remains lower and decreases more rapidly as the day progresses. This situation is explained by the high sensitivity of exergy efficiency to heat quality and the approach of the outlet temperature to the ambient temperature [56].

Considering Fig. 8, the system exhibits its highest and most stable performance between 11:15 and 14:30, during which SR remains

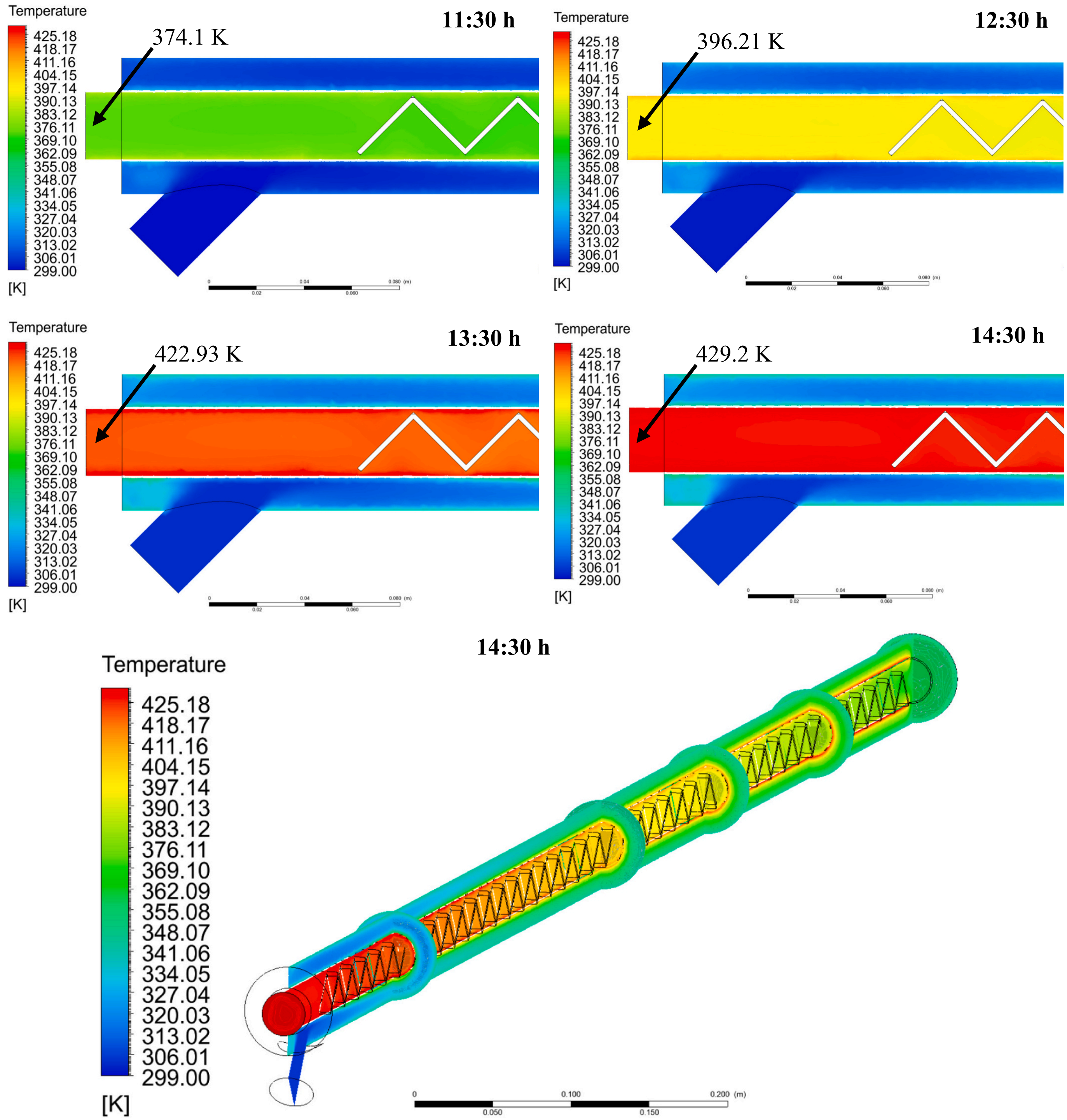

Fig. 12. Temperature distribution contours for the trapezoidal turbulator in CFD analyses.

around ~900 W/m^2 and T_outlet is maintained at ~140–150 °C, leading to plateau values of η_en (~33–35%) and η_ex (~10%). This behavior is mainly attributed to a favorable balance between optical gains and convective–radiative heat losses during midday hours, along with increased useful heat gain at higher outlet temperatures. The literature highlights heat losses as a key factor limiting the efficiency of linear concentrators under varying environmental conditions [57].

The performance drop observed around 14:45–15:05 suggests a short-term meteorological disturbance, such as cloud shading or increased external losses. Previous studies report that wind-induced flow variations and transient shading can significantly affect convective losses and outlet temperature stability in parabolic trough collectors [58]. After 15:00, the rapid decrease of T_outlet toward ambient temperature reduces energy efficiency and further lowers exergy efficiency, consistent with findings that exergy efficiency is more sensitive to temperature levels and generally remains much lower than energy efficiency in solar thermal systems [59].

4.2. Results of uncertainty analysis

The uncertainties related to the calculated key performance parameters were quantified by propagating the uncertainties of the

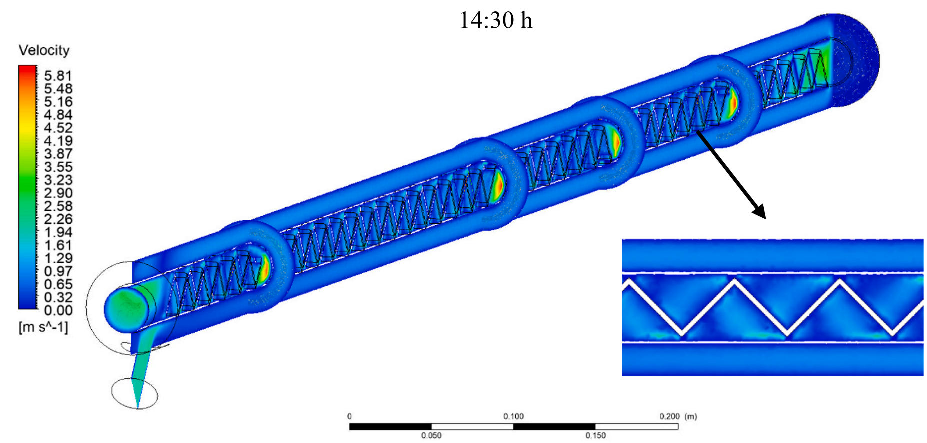

Fig. 13. Air velocity distribution contours for the trapezoidal turbulator in CFD analyses at 14:30.

experimentally measured variables through the relevant equations using the error propagation method. The resulting combined uncertainty values for useful energy gain, energy efficiency, exergy input, exergy loss, and exergy efficiency are summarized in Table 6.

Examination of Table 6 reveals that the uncertainty values remain within an acceptable range; however, DNI-dependent parameters exhibit higher uncertainty because the Erbs-derived DNI introduces an additional model-related component. The relatively low uncertainty in Q_u results from its dependence on directly measured variables, such as temperature difference and mass flow rate. In contrast, the slightly higher uncertainty for η_{en} arises from the inclusion of the DNI variable in its calculation. The uncertainties associated with exergy-based parameters are moderate, reflecting their greater sensitivity to temperature levels and environmental reference conditions. Overall, the observed uncertainty levels demonstrate that the thermal and exergetic performance parameters calculated in this study are reliable.

4.3. Energy-based environmental impact analysis

This study adds an energy-based environmental perspective to conventional PTC performance analyses by quantifying avoided CO_2 emissions. The results show that turbulence generators indirectly reduce emissions by increasing the collector's net useful energy output. Previous studies have primarily focused on thermal behavior and efficiency of PTC receivers using one- and three-dimensional analyses and first- and second-law evaluations, without explicitly addressing avoided emissions [60–63]. To address this limitation, the present work estimates avoided CO_2 from the increase in net output (En_out) obtained with turbulence generators.

As shown in Table 7, the use of a turbulator has increased the estimated annual useful energy output of the PTC system and the associated environmental benefits. While the estimated annual useful energy output was 546,912 Wh/year in the reference case, it increased to 694,580 Wh/year with a helical turbulator and to 661,760 Wh/year with a trapezoidal turbulator. Consequently, the prevented CO_2 emissions were calculated as 0.223 tons/year for the reference system, 0.283 tons/year for the helical turbulator, and 0.270 tons/year for the trapezoidal turbulator. Similarly, the carbon credit value was 3.24 USD/year in the reference case, 4.10 USD/year for the helical turbulator, and 3.91 USD/year for the trapezoidal turbulator. These results indicate that the helical turbulator provides approximately 27% higher net energy output compared to the reference case, while the trapezoidal turbulator provides approximately 21% higher net energy output; environmental indicators also improved in line with this increase.

The annual sunshine duration presented in Table 7 does not correspond to the specific duration of the three experimental days. Instead, the experimentally measured collector performance was annualized using the long-term average sunshine duration for Tokat to avoid overrepresenting the September experimental period and to provide a more representative estimate of yearly useful energy output and CO_2 mitigation potential.

4.4. CFD Findings (Mesh Independence and Numerical Validation)

To ensure the reliability of the CFD results, mesh independence and numerical validation were conducted. Different mesh resolutions were tested by comparing key output parameters, and the experimental PTC outlet temperature was analyzed via CFD at four time intervals between 11:30 and 14:30 (Fig. 9).

Fig. 9 compares CFD-predicted outlet temperatures at various mesh resolutions with experimental outlet-temperature data. Each mesh configuration exhibits the same increasing temperature trend observed experimentally between 11:30 and 14:30, demonstrating that the applied solar heat-flux boundary conditions effectively capture the thermal response of the parabolic trough collector (PTC) during the validation period. The trend lines indicate strong agreement between numerical and experimental results, with R^2 values of 0.9699, 0.9691, and 0.9681 for Type-1, Type-2, and Type-3 meshes, respectively. While all mesh types yield acceptable agreement, the Type-1 mesh achieves the closest correspondence with experimental data due to its finer resolution and enhanced near-wall representation. Consequently, the Type-1 mesh was selected for subsequent CFD analyses.

The error bars represent the uncertainty range associated with the experimental outlet-temperature measurements. The CFD results predominantly fall within or near these uncertainty limits, supporting the reliability of the numerical model for the selected stable, high-radiation period. However, since the validation was restricted to the 11:30–14:30 interval, the reported agreement should not be generalized to low-radiation morning or late-afternoon conditions without additional validation.

As shown in Fig. 9, CFD results for three different mesh models are presented for the experimental data on the outlet temperature of the PTC. The differences between the experimental and CFD analysis results are compared using MAE (Mean Absolute Error) and RMSE (Root Mean Square Error) values, as shown in Table 8.

Type-1 mesh exhibits the lowest error values (MAE $=$ 0.85, RMSE $=$ 0.86), indicating the highest accuracy and best agreement with experimental data. For Type-2, the increased errors (MAE $\approx$ 2.04, RMSE $\approx$ 2.07) suggest moderate deviations, while Type-3 shows the poorest performance with the highest errors (MAE $\approx$ 3.96, RMSE $\approx$ 3.99). Overall, Type-1 provides the most consistent predictions and was therefore selected for subsequent analyses. Based on this selection, CFD results for four time intervals between 11:30 and 14:30 using the Type-1 mesh are presented in Fig. 10. The CFD validation was conducted during

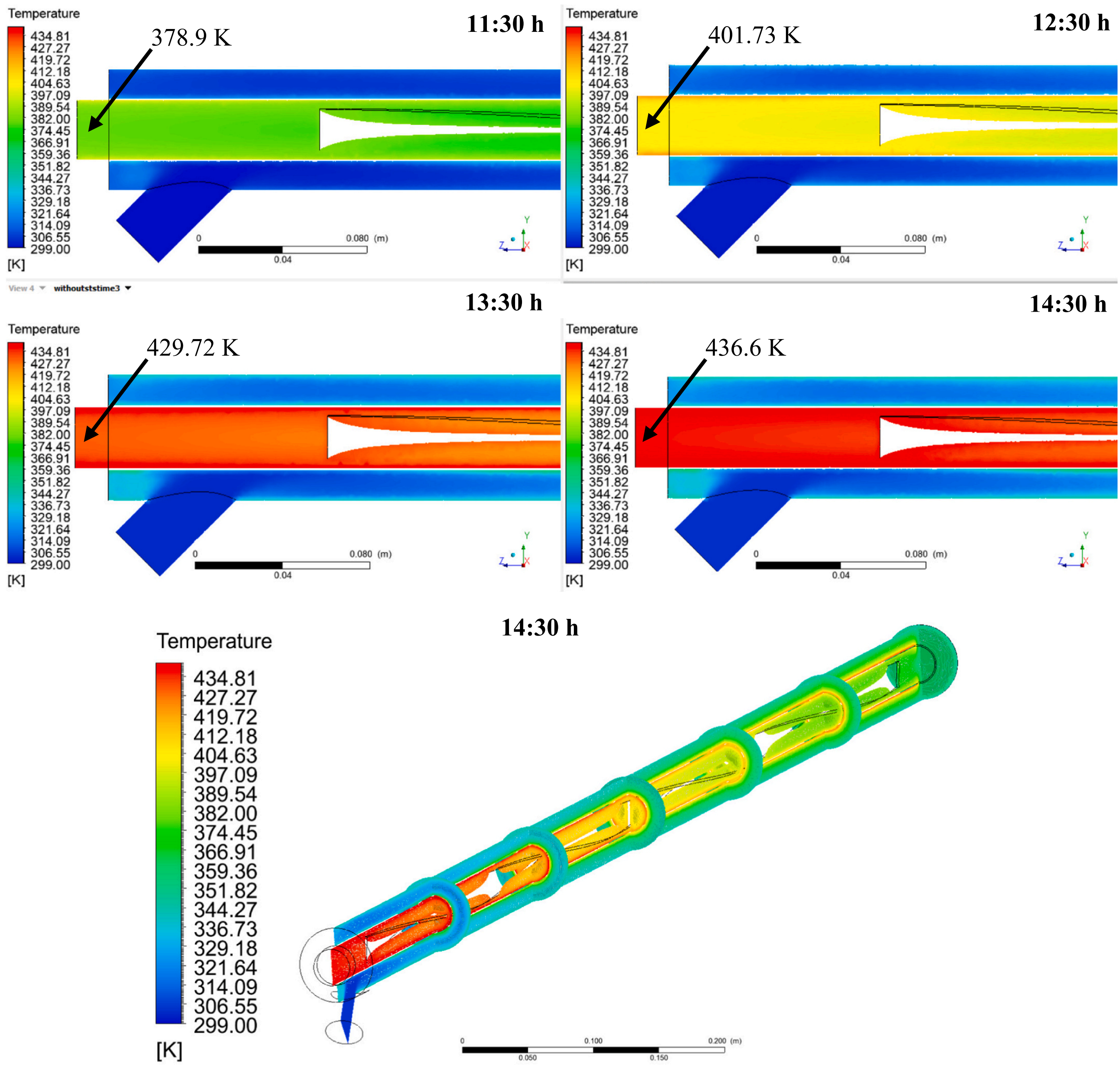

Fig. 14. Temperature distribution contours for the helical turbulator in CFD analyses.

a stable, high-radiation period from 11:30 to 14:30. Therefore, it's important to note that the validation's accuracy may not apply to low-radiation conditions observed in the morning or late afternoon without further validation efforts.

Fig. 10 shows that the outlet temperature increases with solar radiation, becoming more uniform toward noon, which indicates peak thermal performance. Fig. 11 presents the velocity distribution, with maximum velocity at the pipe center and minimum near the walls, forming a parabolic profile due to viscous effects.

In the second part of the CFD analysis, trapezoidal and helical turbulators were placed inside the PTC and repeated under the same conditions. The PTC analysis results using the trapezoidal turbulator are shown in Fig. 12 **and** Fig. 13.

Fig. 12 shows the temperature distributions obtained at different times in the PTC with a trapezoidal turbulator. Toward midday, the outlet temperature increased, the boundary layer weakened due to flow induced by the turbulator, and the temperature distribution became more homogeneous. This enhancement is mainly associated with boundary-layer disruption and stronger fluid mixing induced by the internal turbulators. CFD results demonstrate that the trapezoidal turbulator enhances heat transfer and improves the collector's thermal performance.

Fig. 13 shows the velocity distribution in the PTC at 14:30, with maximum velocity at the pipe center and minimum near the walls, while the turbulator induces vortices and local velocity variations. Fig. 14 **and** Fig. 15 present the CFD results for the helical turbulator, showing increased outlet temperature with rising solar radiation and more uniform temperature distributions due to enhanced mixing and heat transfer, indicating higher efficiency than the conventional design. This behavior is mainly attributed to the stronger secondary flow, enhanced fluid mixing, and more effective disruption of the thermal boundary layer induced by the helical geometry, which together promote

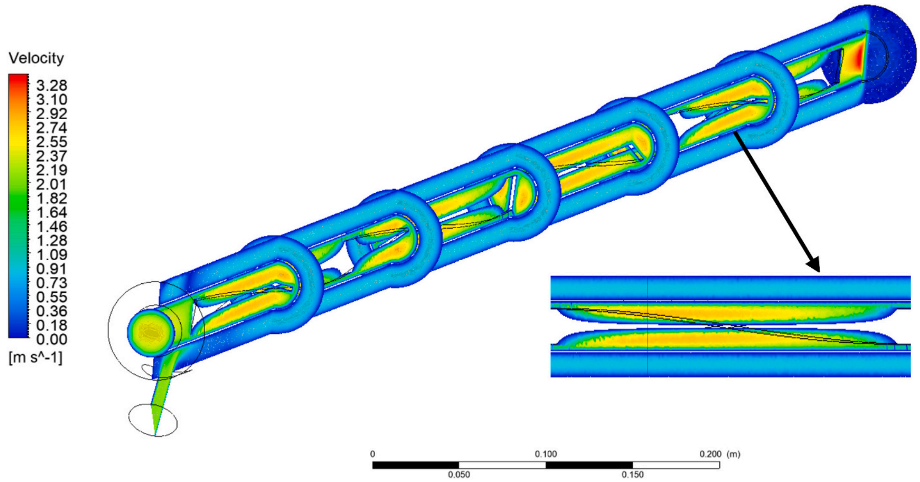

Fig. 15. Air velocity distribution contours for the helical turbulator in CFD analyses at 14:30.

Table 9
Output temperature increases of PTC using turbulators.

Test Time	Temperature increase at the outlet of the trapezoidal turbulator (%)	Temperature increase at the outlet of the helical turbulator (%)
11.30	+3.0%	+7.9%
12.30	+4.6%	+9.2%
13.30	+2.5%	+7.1%
14.30	+3.9%	+8.8%

convective heat transfer inside the absorber tube.

Fig. 15 presents the velocity distribution results for PTC. The development of the fluid velocity profile from inlet to outlet along the collector at 14:30 is clearly visible. According to the analysis results, the fluid enters the system at a relatively low velocity at the collector inlet, and the velocity profile develops as it progresses along the tube. The helical turbulators placed inside the collector smooth the flow, creating vortices and sudden speed changes. The increased number of turbulators used relative to the outlet temperature is given in Table 9.

CFD results indicate that the helical turbulator achieved a higher outlet-temperature-based thermal performance compared to the trapezoidal turbulator. Consequently, the helical turbulator geometry was chosen for physical fabrication and subsequent experimental evaluation. Fig. 16 presents the manufacturing process of the helical turbulator, its installation within the absorber tube, and its integration into the experimental PTC system. These images confirm that the selected geometry is viable for both numerical analysis and experimental implementation.

As shown in Fig. 16(a), a helical turbulator was fabricated and placed inside the absorber tube. The absorber tube assembly was then placed inside a glass tube and evacuated to achieve the final experimental configuration, as shown in Fig. 16(b). Experimental data obtained from the helical turbulator-equipped PTC system under real-world environmental conditions were subsequently used to develop AI-based outlet temperature prediction models. Thus, the machine learning models were trained and evaluated based not only on CFD-generated data but also on experimental data from the fabricated helical turbulator configuration.

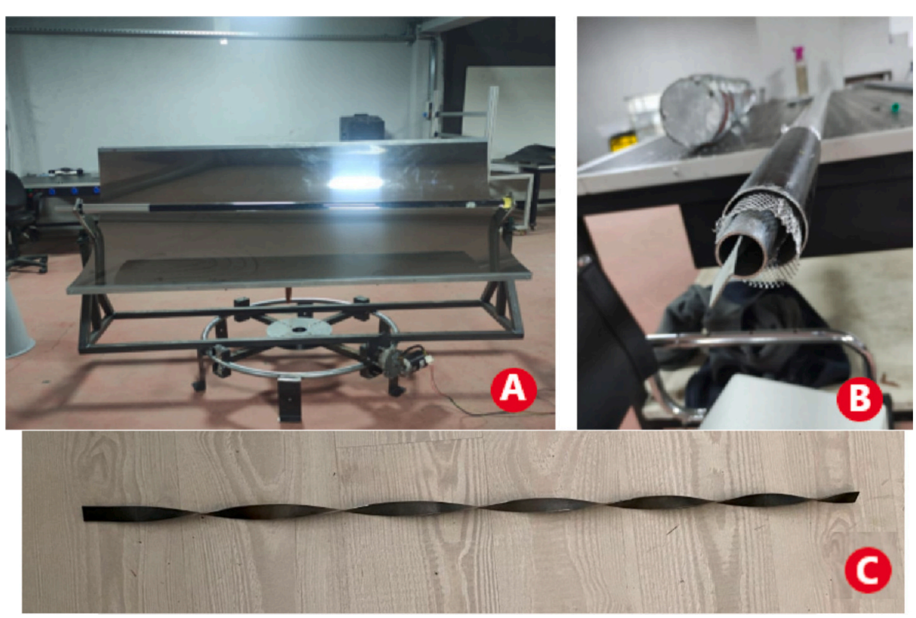

Fig. 16. Manufacturing and experimental integration of the helical-turbulator PTC system: (A) experimental setup, (B) placement of the helical turbulator inside the absorber tube before vacuuming, and (C) manufactured helical turbulator.

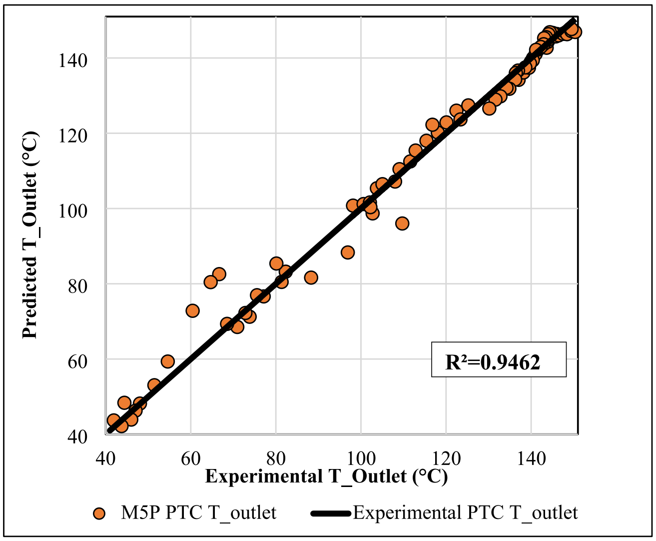

Fig. 17. M5P algorithm model results.

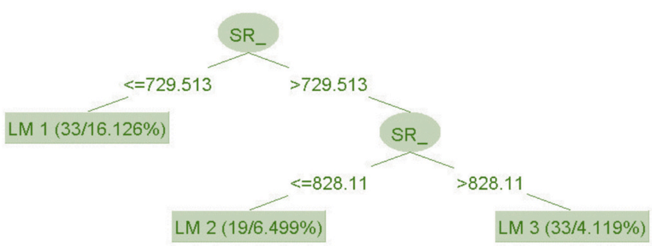

Fig. 18. M5P tree structure.

Table 10
M5P algorithm tree branches (LM) equations.

Tree Branch No	Equation
LM1	T_outlet_PTC = 2.5715 * RH + 0.1481 * SR + 5.9894 * T_a – 3.0089 * WS - 267.8287
LM2	T_outlet_PTC = -0.5489 * RH + 0.1867 * SR + 0.7518 * T_a- 0.3642 * WS - 26.4031
LM3	T_outlet_PTC = 0.0104 * RH + 0.1617 * SR + 0.7518 * T_a – 0.3642 * WS - 22.2253

4.5. Results of Artificial Intelligence

This section presents the results of artificial intelligence models developed to quickly and reliably predict the outlet temperature of a helical turbulator-equipped PTC system based on environmental parameters.

In this study, the experimental dataset used in the artificial intelligence models was obtained from a PTC system equipped with a helical turbulator. Helical and trapezoidal turbulators were first compared using CFD analyses; since the helical turbulator showed a greater increase in outlet temperature and higher outlet-temperature-based thermal response, it was manufactured and installed in the experimental system. Therefore, the model comparisons in Fig. 17 and Fig. 19 show the experimental outlet temperatures from the helical turbulator system alongside the AI model predictions. The trapezoidal turbulator, however, was not included in the AI modeling because no separate experimental dataset was available; instead, it was evaluated within the scope of the experimentally validated CFD model.

Fig. 17 shows that the M5P model predicts the outlet temperature of the helical turbulator-equipped PTC with high accuracy ($R^2 = 0.95$), as most predictions align closely with experimental data. The decision tree in Fig. 18 identifies solar radiation (SR) as the dominant parameter and defines three linear submodels (LM1–LM3) for different radiation levels, indicating regime-dependent thermal behavior. The corresponding regression equations are provided in Table 10, demonstrating that M5P combines accurate prediction with physical interpretability.

Table 10 shows that the M5P model captures the PTC outlet temperature across three solar-radiation-based regimes (LM1–LM3), confirming its physical interpretability.

The LM1–LM3 branches in the M5P model represent the system's varying thermal behavior under different solar radiation and environmental conditions. The fact that the solar radiation coefficient is positive in all submodels indicates that the amount of useful heat transferred from the absorber surface to the air increases with rising radiation. The positive effect of ambient temperature can be attributed to the system reaching a higher outlet temperature at higher inlet/ambient temperatures. Conversely, the negative wind speed coefficient indicates that the outlet temperature may decrease due to increased convective heat losses to the external environment. Relative humidity coefficients, however, should be evaluated not as a direct heat transfer mechanism but as a statistical effect that varies alongside other meteorological variables within the limited outdoor ambient data set. Therefore, the M5P model not only provides high prediction accuracy but also clearly illustrates the relative effects of environmental variables on PTC outlet temperature across different operating regimes.

The positive coefficient of relative humidity in the Elastic.Net equation should not be interpreted as a direct physical enhancement of heat transfer. This coefficient most likely reflects the statistical structure of the limited outdoor dataset, where relative humidity may covary with solar radiation, ambient temperature, and time-dependent meteorological conditions. Therefore, RH can be considered a proxy variable for the combined environmental state rather than an independent causal factor increasing the outlet temperature. This also explains why the piecewise M5P model provides more physically consistent and accurate predictions than the single linear Elastic.Net formulation.

Fig. 19 indicates that the Elastic.Net model provides a reasonable fit to experimental data ($R^2 = 0.8962$), although larger deviations occur at low–medium temperatures due to its single linear structure. Overall, while Elastic.Net offers satisfactory accuracy, M5P performs better by representing regime-dependent thermal behavior.

Table 11 shows the Elastic.Net regression equation, which indicates

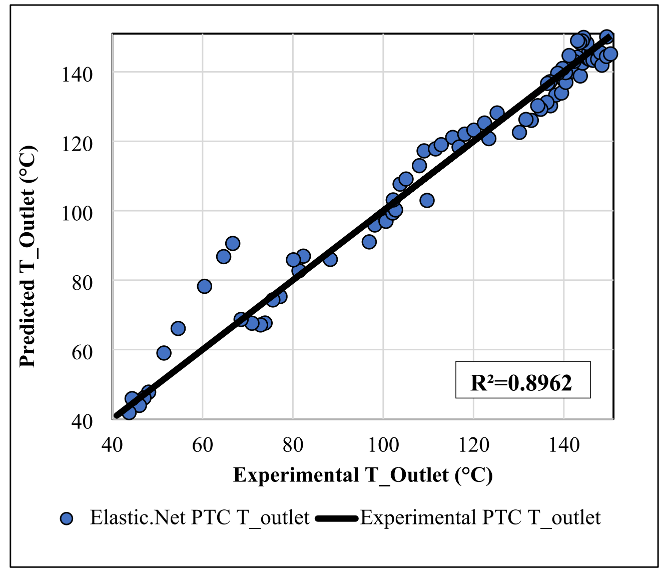

Fig. 19. Elastic.Net model results.

Table 11
PTC outlet temperature equation obtained with the Elastic.Net algorithm.

Elastic.Net regression model equation
T_outlet_PTC = 1.046 * RH - 156.4964 + 0.1837 * SR + 3.3579 * T_a − 1.6268 * WS

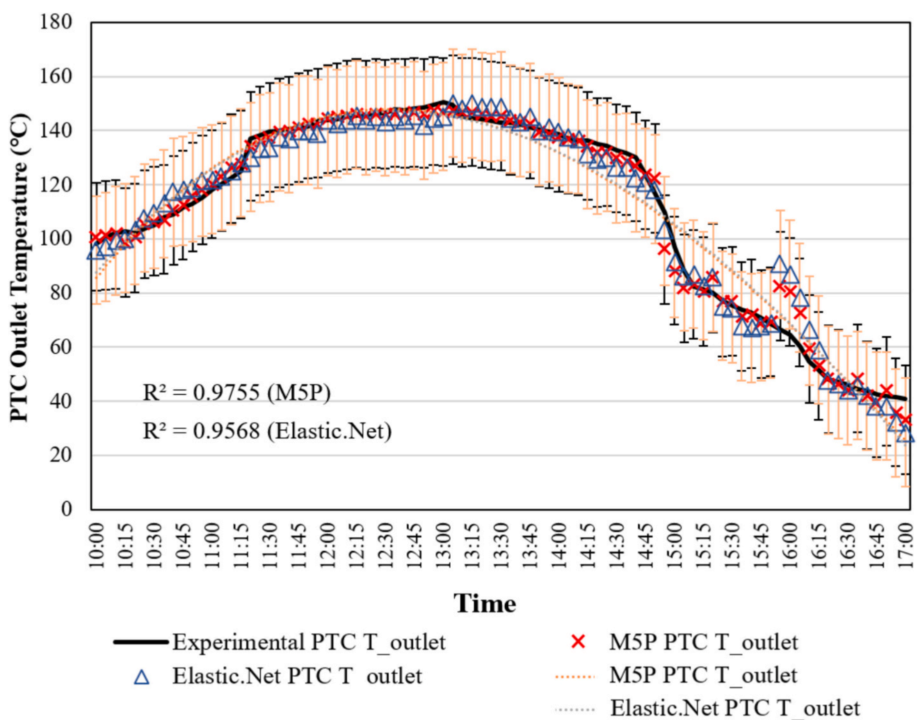

Fig. 20. Comparison of all machine learning algorithm results with experimental PTC outlet temperature results.

Table 12
Statistical error analysis results of machine learning methods.

Model Parameters	MAE	RMSE	RAE
M5P	0.256	0.4043	8.37%
Elastic.Net	0.432	1.5325	14.11%

that the PTC outlet temperature (T_outlet_PTC) varies with relative humidity (RH), solar radiation (SR), ambient temperature (T_a), and wind speed (WS), and that these variables together significantly explain the outlet temperature.

The positive SR (0.1837·SR) and ambient temperature (3.3579·T_a) coefficients indicate increased net heat gain and outlet temperature with higher irradiance and ambient temperature, consistent with PTC thermal performance trends reported in the literature [64,65]. Conversely, the negative wind speed coefficient (−1.6268·WS) reflects enhanced convective heat losses at higher wind speeds, leading to reduced outlet temperature [66]. The positive RH coefficient (1.046·RH) suggests a statistical association with outlet temperature, likely acting as a proxy for irradiance variability rather than a direct thermal effect [67].

Consequently, the positive RH coefficient in the Elastic.Net equation should be interpreted solely within the context of the regression coefficient structure of the developed model, rather than as evidence of a direct causal thermal effect. The coefficient sign reflects the statistical relationship identified from the limited three-day dataset, in which RH may covary with irradiance variability, ambient temperature, and other time-dependent meteorological variables. Therefore, the Elastic.Net coefficients were used exclusively to enhance model interpretability within the available dataset and not to establish independent physical causality.

The predictive performance of the models was evaluated using time-series comparisons (Fig. 20) and error metrics (Table 12). As shown in Fig. 20, the M5P model closely follows experimental outlet temperature variations, particularly during rapid transitions, whereas the Elastic.Net model captures the general trend but exhibits larger deviations. This difference arises from the piecewise structure of M5P, which more effectively represents regime-dependent behavior.

The time-series comparison in Fig. 20 presents the experimental PTC outlet-temperature results together with the corresponding AI-based prediction results at the same time points. The experimental measurements were recorded for 420 min at 5-min intervals, resulting in 84 comparison points. Therefore, Fig. 20 provides a point-by-point comparison between the measured outlet temperature and the predicted values obtained from the AI models under the same outdoor operating period.

Fig. 20 compares the time-dependent experimental PTC outlet temperature with predictions from the M5P and Elastic.Net models. Both models replicate the experimental trend during the heating, peak-temperature, and cooling phases. The M5P model shows slightly better alignment with the experimental data, as reflected in its higher R^2 of 0.9755 compared to Elastic.Net's 0.9568. Deviations become more pronounced during the rapid temperature decline after approximately 14:45, likely due to transient meteorological effects that may have increased prediction error. In summary, the error bars and trend lines suggest that both artificial intelligence models effectively capture the temporal dynamics of the PTC outlet temperature, with M5P yielding more accurate predictions.

The error analysis results in Table 12 numerically confirm this visual finding: The M5P model produced the lowest error values with MAE = 0.256, RMSE = 0.4043, and RAE = 8.37%, while the Elastic.Net model

Table 13
Recent studies on parabolic trough solar collector performance enhancement and comparison with the present study.

Reference	System / method	Enhancement method	Difference from present study
[17]	PTC, 3D numerical CFD	Inserted fins with increasing fin number and different fin cross-sections	Present study investigates helical and trapezoidal turbulators, not fin arrays; also includes experimental validation + interpretable AI
[68]	SPTC, experimental heat-transfer study	Corrugated tube receiver + conical strip inserts	Present study uses air and compares two internal turbulator geometries in the same framework rather than corrugated tube + conical strip combinations
[6]	PTC receiver, CFD	Innovative receiver configurations	Present study does not use nanofluid; it focuses on air-based PTC with passive internal turbulators and includes experiments
[69]	PTSC, modeling + validation	Twisted/helical fin integration	Present study compares helical vs trapezoidal turbulators and supports the analysis with measured outlet-temperature data and AI prediction
[70]	SPTC, machine-learning prediction study	Corrugated tube receiver concept + ML prediction	Present study uses interpretable AI (M5P + Elastic.Net) together with experimental and CFD results, not ML alone
[71]	PTC, numerical study	Novel turbulator	Present study emphasizes experimental validation, air-based operation, and interpretable AI-based outlet-temperature prediction, not only numerical enhancement

showed higher deviations with MAE = 0.432, RMSE = 1.5325, and RAE = 14.11%. Therefore, when both time series fit and error metrics are evaluated together, it is concluded that the M5P model is the most successful approach for predicting PTC outlet temperature and produces results closest to the experimental data. Table 13 summarizes recent studies on thermal-performance enhancement in parabolic trough solar collectors, highlighting system types, enhancement methods, and how this work differs from recent numerical, experimental, and data-driven research.

Table 13 shows that recent studies on parabolic trough solar collectors have mainly focused on improving thermal performance through modifications to the receiver tube, the insertion of fins, twisted tapes, innovative internal geometries, hybrid nanofluids, and data-driven design approaches. In general, these studies demonstrate that thermal enhancement can be achieved by promoting fluid mixing, disturbing the thermal boundary layer, or improving the thermophysical behavior of the working fluid. However, many of these studies are limited to numerical analysis, nanofluid-based systems, or optimization-oriented frameworks. In contrast, the present study evaluates helical and trapezoidal turbulators in an air-based PTC system using an integrated framework that combines outdoor experiments, validated three-dimensional CFD analysis, and interpretable AI-based outlet-temperature prediction. Therefore, the main distinction of the present work lies in the comparative assessment of passive internal turbulators under real operating conditions, together with physically interpretable and experimentally supported prediction capability.

5. Limitations of the Study

The main limitations of this study are that the experiments were conducted over a short period, at a single geographical location, and under constant operating conditions. Numerical validation was conducted only within a selected time interval and under limited environmental conditions; therefore, the model is considered to require further validation across a wider range of solar irradiance, ambient temperature, and meteorological conditions. Similarly, in the CFD model, fluid and solid material properties were assumed to be constant; the detailed surface-to-surface radiative interaction between the receiver tube and the glass envelope was not explicitly solved; and thermo-hydraulic behavior, such as pressure drop and fan power increase, was not examined in detail within the scope of this study. Furthermore, no independent parametric analysis has been conducted for geometric and optical parameters such as the pitch of helical and trapezoidal turbulators, the ratio of their covered diameter, and their relationship with the optical focal region.

Additionally, the artificial intelligence models were developed using the existing experimental dataset and selected environmental parameters. Their generalizability to different climate zones and broader operating ranges must be tested in further studies. The CO_2 emission factor in the environmental assessment was updated to a more representative regional value based on available literature. This approach still depends on a specific grid scenario, so results may vary across different countries and energy mixes. The scope of the study could be expanded in the future to include long-term and multi-climate experiments, transient regime CFD analyses, advanced turbulator geometries, thermo-hydraulic performance evaluations, and region-specific environmental sensitivity analyses.

6. Conclusions

This study integrates experimental measurements, CFD-based numerical analyses, and interpretable artificial intelligence models to enhance the performance of parabolic trough solar collectors (PTC). Experiments conducted under Tokat climate conditions provided reliable data for energy–exergy evaluation and CFD validation, with the developed 3D model accurately predicting outlet temperature during the selected stable high-radiation validation period (MAE ≈ 0.85 °C, RMSE ≈ 0.86 °C). The use of helical and trapezoidal turbulators improved flow mixing and increased outlet temperature by 7–9% and 3–5%, respectively. The helical turbulator provided the highest outlet-temperature-based thermal performance by producing a greater outlet-temperature increase and higher annual useful energy output than the trapezoidal turbulator. Among the AI models, the M5P decision tree achieved the highest accuracy ($R^2 \approx 0.95$) and revealed solar radiation and ambient temperature as dominant factors, with wind speed having a negative effect due to heat losses. Enhanced useful energy output also increased the environmental benefit, raising the annual CO_2 reduction from approximately 0.223 ton/year to 0.283 ton/year for the helical turbulator. The results indicate that the experimental–CFD–AI framework offers significant potential for enhancing the outlet-temperature-based performance of air-based PTC systems under the specific operating conditions tested. However, these findings are condition-specific and reflect the Tokat climate, the selected validation period, and the three-day experimental dataset. Comprehensive validation across multiple seasons, a wider range of irradiance levels, variable mass flow rates, and longer operating periods is necessary before broader generalization or scale-up can be justified.

The combined experimental–CFD–AI framework provides an integrated evaluation of the proposed system, the results should be interpreted within the assumptions and operating conditions considered in the present study. Nevertheless, the proposed approach is particularly applicable to air-based solar thermal systems such as drying, process-air heating, and medium-temperature heat-recovery applications, where the reported enhancement in outlet-air temperature and useful energy output can improve thermal process effectiveness, reduce auxiliary energy demand, and support more efficient utilization of concentrated solar energy.

Declaration of competing interest

The authors declare that they have no known competing financial interests or personal relationships that could have appeared to influence the work reported in this paper.

Acknowledgments

This study was supported by the Tokat Gaziosmanpaşa University (TOGU) - Scientific Research Projects Coordination Unit under Grant Number 2022/46 and Fırat University Scientific Research Projects Coordinatorship (FUBAP) (Projects No. MF.25.78). The authors thank TOGU and FUBAP for their support.

Appendix A. Supplementary data

Supplementary data to this article can be found online at https://doi.org/10.1016/j.applthermaleng.2026.131854.

Data availability

The authors do not have permission to share data.

References

[1] A.A. Rabienataj Darzi, M. Razbin, A. Allahdadi, S.M. Mousavi, R.A. Taylor, M. Li, Designing high-efficiency parabolic trough receiver tubes via AI-assisted simulation, Renew. Energy 251 (2025) 123366, https://doi.org/10.1016/j.renene.2025.123366.
[2] R.K.R.K.K. Pal, Investigations of thermo-hydrodynamics, structural stability, and thermal energy storage for direct steam generation in parabolic trough solar collector: A comprehensive review, J. Clean. Prod. 311 (2021) 127550, https://doi.org/10.1016/j.jclepro.2021.127550.
[3] Z.D. Cheng, Y.L. He, B.C. Du, K. Wang, Q. Liang, Geometric optimization on optical performance of parabolic trough solar collector systems using particle swarm optimization algorithm, Appl. Energy 148 (2015) 282–293, https://doi.org/10.1016/j.apenergy.2015.03.079.
[4] A. Malan, K. Ravi Kumar, A comprehensive review on optical analysis of parabolic trough solar collector, Sustain. Energy Technol. Assess. 46 (2021) 101305, https://doi.org/10.1016/j.seta.2021.101305.
[5] Y. Xiong, Y. Wu, C. Ma, M.K. Traore, Y. Zhang, Numerical investigation of thermal performance of heat loss of parabolic trough receiver, Sci. China Technol. Sci. 53 (2010) 444–452, https://doi.org/10.1007/s11431-009-0279-x.
[6] J. Byiringiro, M. Chaanaoui, M. Halimi, Heat transfer enhancement of a parabolic trough solar collector using innovative receiver configurations combined with a hybrid nanofluid: CFD analysis, Renew. Energy 233 (2024) 121169, https://doi.org/10.1016/j.renene.2024.121169.
[7] A. Khanlari, H.Ö. Güler, A.D. Tuncer, C. Şirin, Y.C. Bilge, Y. Yılmaz, A. Güngör, Experimental and numerical study of the effect of integrating plus-shaped perforated baffles to solar air collector in drying application, Renew. Energy 145 (2020) 1677–1692, https://doi.org/10.1016/j.renene.2019.07.076.
[8] V.P. Kalbande, P.V. Walke, S. Untawale, M. Mohan, Performance evaluation of novel heat pipe-assisted thermal storage system with parabolic trough solar collector using Nanofluid, Energy Technol. 10 (2022) 1–14, https://doi.org/10.1002/ente.202200118.
[9] V.P. Kalbande, P.V. Walke, K. Rambhad, Performance of oil-based thermal storage system with parabolic trough solar collector using Al2O3 and soybean oil nanofluid, Int. J. Energy Res. 45 (2021) 15338–15359, https://doi.org/10.1002/er.6808.
[10] V.P. Kalbande, P.V. Walke, R. Shelke, Aluminum-based thermal storage system with solar collector using nanofluid, Energy Storage 1 (2019) 1–7, https://doi.org/10.1002/est2.99.
[11] K. Ravi Kumar, K.S. Reddy, Effect of porous disc receiver configurations on performance of solar parabolic trough concentrator, Heat Mass Transf. 48 (2012) 555–571, https://doi.org/10.1007/s00231-011-0903-8.
[12] A. Mwesigye, T. Bello-Ochende, J.P. Meyer, Heat transfer and entropy generation in a parabolic trough receiver with wall-detached twisted tape inserts, Int. J. Therm. Sci. 99 (2016) 238–257, https://doi.org/10.1016/j.ijthermalsci.2015.08.015.
[13] H.A. Mohammed, H.B. Vuthaluru, S. Liu, Heat transfer augmentation of parabolic trough solar collector receiver's tube using hybrid nanofluids and conical turbulators, J. Taiwan Inst. Chem. Eng. 125 (2021) 215–242, https://doi.org/10.1016/j.jtice.2021.06.032.
[14] S. Ghadirijafarbeigloo, A.H. Zamzamian, M. Yaghoubi, 3-D numerical simulation of heat transfer and turbulent flow in a receiver tube of solar parabolic trough concentrator with louvered twisted-tape inserts, Energy Procedia 49 (2014) 373–380, https://doi.org/10.1016/j.egypro.2014.03.040.
[15] P. Liu, N. Zheng, Z. Liu, W. Liu, Thermal-hydraulic performance and entropy generation analysis of a parabolic trough receiver with conical strip inserts, Energy Convers. Manag. 179 (2019) 30–45, https://doi.org/10.1016/j.enconman.2018.10.057.
[16] X. Liu, M.V. Bozorg, Q. Xiong, W. Li, Numerical analysis of a new design strategy for parabolic trough solar collectors for improved production and consumption of solar energy in the belt and road initiative countries, J. Clean. Prod. 367 (2022) 133079, https://doi.org/10.1016/j.jclepro.2022.133079.
[17] W. Al-Aloosi, Y. Alaiwi, H. Hamzah, Thermal performance analysis in a parabolic trough solar collector with a novel design of inserted fins, Case Stud. Therm. Eng. 49 (2023) 103378, https://doi.org/10.1016/j.csite.2023.103378.
[18] E.K. Amal, E.A. Oumaima, A. Elhassan, CFD simulation of temperature distribution in a parabolic trough collector, Appl. Sol. Energy (English Transl. Geliotekhnika) 59 (2023) 311–323, https://doi.org/10.3103/S0003701X23600303.
[19] J. Byiringiro, M. Chaanaoui, M. Halimi, Heat transfer enhancement of a parabolic trough solar collector using innovative receiver configurations combined with a hybrid nanofluid: CFD analysis, Renew. Energy 233 (2024) 121169, https://doi.org/10.1016/j.renene.2024.121169.
[20] W. Al-Aloosi, Y. Alaiwi, H. Hamzah, Thermal performance analysis in a parabolic trough solar collector with a novel design of inserted fins, Case Stud. Therm. Eng. 49 (2023) 103378, https://doi.org/10.1016/j.csite.2023.103378.
[21] A.A. Rabienataj Darzi, M. Razbin, A. Allahdadi, S.M. Mousavi, R.A. Taylor, M. Li, Designing high-efficiency parabolic trough receiver tubes via AI-assisted simulation, renew, Energy 251 (2025) 123366, https://doi.org/10.1016/j.renene.2025.123366.
[22] Seung-min Lee, Hye-rin Park, Computational and data-driven integration for sustainable solar thermal collector design, Front. Artif. Intell. Res. 2 (2025) 385–398, https://doi.org/10.71465/fair322.
[23] A. Alhamayani, Performance analysis and machine learning algorithms of parabolic trough solar collectors using Al2O3-MWCNT as a hybrid nanofluid, Case Stud. Therm. Eng. 57 (2024) 104321, https://doi.org/10.1016/j.csite.2024.104321.
[24] R.K. Kottala, K.R. Balasubramanian, B.S. Jinshah, S. Divakar, B.K. Chigilipalli, Experimental investigation and machine learning modelling of phase change material-based receiver tube for natural circulated solar parabolic trough system under various weather conditions, J. Therm. Anal. Calorim. 148 (2023) 7101–7124, https://doi.org/10.1007/s10973-023-12219-9.
[25] X. Hu, L. Guo, J. Wang, Y. Liu, Computational fluid dynamics and machine learning integration for evaluating solar thermal collector efficiency -based parameter analysis, Sci. Rep. 15 (2025) 1–21, https://doi.org/10.1038/s41598-025-10212-w.
[26] İ.H. Yılmaz, A. Mwesigye, F. Kılıç, Prioritization of heat transfer fluids in parabolic trough solar systems using CFD-assisted AHP-VIKOR approach, Renew. Energy 210 (2023) 751–768, https://doi.org/10.1016/j.renene.2023.04.048.
[27] H.A. Jabbar, K.J. Alwan, D.M. Hachim, A. Al-Manea, R. Al-Rbaihat, A. Alahmer, Comparative assessment of thermal oils and water as working fluids in parabolic trough collectors for enhanced solar power generation, Eng. Res. Express 6 (2024), https://doi.org/10.1088/2631-8695/ad6122.
[28] D.M. Hachim, A.A. Eidan, M.J. Alshukri, M. Al-Fahham, A. Alsahlani, A. Al-Manea, R. Al-Rbaihat, A. Alahmer, Integration of thermal energy storage materials in heat pipe evacuated tube solar collector Systems for Enhanced Solar Thermal Performance, Comput. Therm. Sci. 16 (2024) 59–85, https://doi.org/10.1615/ComputThermalScien.2024053130.
[29] D.G. Erbs, S.A. Klein, J.A. Duffle, Estimation of the diffuse radiation fraction for hourly, daily and monthly-average global radiation, Sol. Energy 28 (1982).
[30] S. Hosouli, L. Jackson-french, G. Pierucci, M. De Lucia, Predicting outdoor performance of solar parabolic trough collector (PTC) from indoor test data using machine learning, Appl. Therm. Eng. 290 (2026) 130020, https://doi.org/10.1016/j.applthermaleng.2026.130020.
[31] M. Tavakoli, M.R. Soufivand, Investigation of entropy generation, PEC, and efficiency of parabolic solar collector containing water/Al2O3−MWCNT hybrid nanofluid in the presence of finned and perforated twisted tape turbulators using a two-phase flow scheme, Eng. Anal. Bound. Elem. 148 (2023) 324–335, https://doi.org/10.1016/j.enganabound.2022.12.022.
[32] S. Husnain, A. Qamar, F. Noor, F. Riaz, M. Usman, M. Farooq, M. Sultan, A. Ur, A. Shahzadi, J.M. Andresen, Case studies in thermal engineering experimental analysis of thermal performance of direct absorption parabolic trough collector integrating water based nanofluids for sustainable environment applications, Case Stud. Therm. Eng. 49 (2023) 103366, https://doi.org/10.1016/j.csite.2023.103366.
[33] B. El, D. Martinez, R. Ait, E. Cadi, A. Ihlal, Thermal plant based on parabolic trough collectors for industrial process heat generation in Morocco, Renew. Energy 113 (2017) 1261–1275, https://doi.org/10.1016/j.renene.2017.06.063.
[34] A.G. Devecioğlu, V. Oruc, Z. Tuncer, Energy and exergy analyses of a solar air heater with wire mesh-covered absorber plate, Int. J. Exergy 26 (2018) 3–20, https://doi.org/10.1504/IJEX.2018.092500.

[35] H. Samimi Akhijahani, P. Salami, M. Iranmanesh, M.S.B. Jahromi, Experimental study on the solar drying of rhubarb (Rheum ribes L.) with parabolic trough collector assisted with air recycling system, nanofluid and energy storage system, J. Energy Storage 60 (2023) 106451, https://doi.org/10.1016/j.est.2022.106451.
[36] O. Onenli, H. Ercan, S. Acikgoz, B. Kat, Emission reduction pathways for satisfying Türkiye's future electricity demand: a cross-country dynamic panel analysis with linear programming scenarios, Cleaner Energy Syst. 6 (2023) 100085, https://doi.org/10.1016/j.cles.2023.100085.
[37] H. Hassan, M.S. Yousef, S. Abo-Elfadl, Energy, exergy, economic and environmental assessment of double pass V-corrugated-perforated finned solar air heater at different air mass ratios, Sustain. Energy Technol. Assess. 43 (2021) 100936, https://doi.org/10.1016/j.seta.2020.100936.
[38] D. Evin, A. Uçar, Investigation of the temperature distribution of a small solar chimney, Eur. J. Sci. Technol. (2019) 109–116, https://doi.org/10.31590/ejosat.582533.
[39] Turkish State Meteorological Service, Cities & Holiday Resorts, Forecast cities, Tokat, 2026. https://www.mgm.gov.tr/eng/forecast-cities.aspx?m=TOKAT. accessed May 8, 2026.
[40] M.S. Yousef, H. Hassan, Energy payback time, exergoeconomic and enviroeconomic analyses of using thermal energy storage system with a solar desalination system: an experimental study, J. Clean. Prod. 270 (2020) 122082, https://doi.org/10.1016/j.jclepro.2020.122082.
[41] J.P. Holman, Experimental Methods for Engineers, Eight Edit, McGraw-Hill, New York, 2012.
[42] A. Sarangi, A. Sarangi, S.S. Sahoo, R.K. Mallik, S. Ray, S.M. Varghese, A review of different working fluids used in the receiver tube of parabolic trough solar collector, J. Therm. Anal. Calorim. 148 (2023) 3929–3954, https://doi.org/10.1007/s10973-023-11991-y.
[43] S. Ray, A.K. Tripathy, S.S. Sahoo, H. Bindra, Performance analysis of receiver of parabolic trough solar collector: effect of selective coating, vacuum and semitransparent glass cover, Int. J. Energy Res. 42 (2018) 4235–4249, https://doi.org/10.1002/er.4137.
[44] A.H. Al-Tohamy, O.A. Ismail, A. Kaood, Hydrothermal performance evaluation of parabolic trough collector with conical dimpled receiver, J. Therm. Anal. Calorim. 150 (2025) 6259–6286, https://doi.org/10.1007/s10973-025-14115-w.
[45] H. Ma, P. Liu, L. Huang, Y. Ge, L. Chen, Performance analysis and heat transfer multi-objective optimization of parabolic trough receiver with annular sector inserts, Sci. China Technol. Sci. 68 (2025) 1–18, https://doi.org/10.1007/s11431-024-2807-y.
[46] A. Fluent, ANSYS Fluent Theory Guide 15.0, ANSYS, Canonsburg, PA, 2013.
[47] A. Kaood, O.A. Ismail, A.H. Al-Tohamy, Hydrothermal performance assessment of a parabolic trough with proposed conical solar receiver, Renew. Energy 222 (2024) 119939, https://doi.org/10.1016/j.renene.2024.119939.
[48] H. Hamzah, B. Sahin, Analysis of SWCNT-water nanofluid flow in wavy channel under turbulent pulsating conditions: investigation of homogeneous and discrete phase models, Int. J. Therm. Sci. 184 (2023) 108011, https://doi.org/10.1016/j.ijthermalsci.2022.108011.
[49] A. Sözen, C. Şirin, A. Khanlari, A.D. Tuncer, E.Y. Gürbüz, Thermal performance enhancement of tube-type alternative indirect solar dryer with iron mesh modification, Sol. Energy 207 (2020) 1269–1281, https://doi.org/10.1016/j.solener.2020.07.072.
[50] O.E. Akay, M. Das, Modeling the total heat transfer coefficient of a nuclear research reactor cooling system by different methods, Case Stud. Therm. Eng. 25 (2021) 100914, https://doi.org/10.1016/j.csite.2021.100914.
[51] J. Hatamiafkoueieh, S. Heddam, S. Khoshtinat, S. Khazaei, A.B. Osmani, E. Nohani, M. Kiomarzi, E. Sharafi, J. Tiefenbacher, Enhanced forecasting of multi-step ahead daily soil temperature using advanced hybrid vote algorithm-based tree models, J. Hydroinf. 25 (2023) 2643–2659, https://doi.org/10.2166/hydro.2023.188.
[52] H. Zou, T. Hastie, Erratum: Regularization and variable selection via the elastic net (Journal of the Royal Statistical Society. Series B: Statistical Methodology (2005) 67 (301−320)), J. R. Stat. Soc. Ser. B Stat. Methodol 67, 2005, p. 768, https://doi.org/10.1111/j.1467-9868.2005.00527.x.
[53] J.O. Ogutu, T. Schulz-Streeck, H.P. Piepho, Genomic selection using regularized linear regression models: ridge regression, BMC Proc. 6 (2012) S10.
[54] E. Arslan, Applying regression techniques to determine mathematical equations of exergy, electricity, and energy values of photovoltaic thermal collector, Sol. Energy 255 (2023) 369–380, https://doi.org/10.1016/j.solener.2023.02.020.
[55] M. Das, Innovative renewable energy solutions for antarctic research stations: a case study on the photovoltaic systems in Horseshoe Island, Environ. Technol. Innov. 40 (2025) 104449, https://doi.org/10.1016/j.eti.2025.104449.
[56] M.O. Karaağaç, B. Akıncı, A. Ergün, Enhancing the performance of parabolic trough solar collectors: cost-effective innovative designs for sustainable energy harvesting, Appl. Therm. Eng. 253 (2024), https://doi.org/10.1016/j.applthermaleng.2024.123693.
[57] A. Ahmad, O. Prakash, R. Kausher, G. Kumar, S. Pandey, S.M.M. Hasnain, Parabolic trough solar collectors: a sustainable and efficient energy source, Mater. Sci. Energy Technol. 7 (2024) 99–106, https://doi.org/10.1016/j.mset.2023.08.002.
[58] M. Abutayeh, R.V. Padilla, M. Lake, Y.Y. Lim, J. Garcia, M. Sedighi, Y.C. Soo Too, K. Jeong, Effect of short cloud shading on the performance of parabolic trough solar power plants: motorized vs manual valves, Renew. Energy 142 (2019) 330–344, https://doi.org/10.1016/j.renene.2019.04.094.
[59] M. Abou Houran, A.A. Dagestani, T.U.K. Nutakki, A. Albani, A.A. Ifseisi, F. Riaz, F. Peng, Energy and exergy analysis of a novel solar-based system merged with power cycle, Appl. Therm. Eng. 240 (2024) 122080, https://doi.org/10.1016/j.applthermaleng.2023.122080.
[60] J. Guo, X. Huai, Z. Liu, Performance investigation of parabolic trough solar receiver, Appl. Therm. Eng. 95 (2016) 357–364, https://doi.org/10.1016/j.applthermaleng.2015.11.035.
[61] R.V. Padilla, G. Demirkaya, D.Y. Goswami, E. Stefanakos, M.M. Rahman, Heat transfer analysis of parabolic trough solar receiver, Appl. Energy 88 (2011) 5097–5110, https://doi.org/10.1016/j.apenergy.2011.07.012.
[62] Z. Wu, S. Li, G. Yuan, D. Lei, Z. Wang, Three-dimensional numerical study of heat transfer characteristics of parabolic trough receiver, Appl. Energy 113 (2014) 902–911, https://doi.org/10.1016/j.apenergy.2013.07.050.
[63] J.D. Osorio, A. Rivera-Alvarez, Performance analysis of parabolic trough collectors with double glass envelope, Renew. Energy 130 (2019) 1092–1107, https://doi.org/10.1016/j.renene.2018.06.024.
[64] V. Sorel Chara-Dackou, D. Njomo, R. Tchinda, M. Hassane Babikir, Y. Simplice Kondji, Thermal performance analysis of the parabolic trough solar collector in the sub-Saharan climate of the Central African Republic, Sustain. Energy Technol. Assess. 58 (2023), https://doi.org/10.1016/j.seta.2023.103331.
[65] Y. Bie, M. Li, F. Chen, G. Królczyk, Z. Li, Heat transfer mathematical model for a novel parabolic trough solar collecting system with V-shaped cavity absorber, Sustain. Cities Soc. 52 (2020) 101837, https://doi.org/10.1016/j.scs.2019.101837.
[66] A.A. Hachicha, I. Rodríguez, A. Oliva, Wind speed effect on the flow field and heat transfer around a parabolic trough solar collector, Appl. Energy 130 (2014) 200–211, https://doi.org/10.1016/j.apenergy.2014.05.037.
[67] E. Rodríguez, E.L. Droguett, J.M. Cardemil, A.R. Starke, L. Cornejo-Ponce, Enhancing the estimation of direct normal irradiance for six climate zones through machine learning models, Renew. Energy 231 (2024) 120925, https://doi.org/10.1016/j.renene.2024.120925.
[68] R. Venkatesaperumal, K. Syed Jafar, P.V. Elumalai, M. Abbas, E. Cuce, S. Shaik, C. A. Saleel, Heat transfer studies on solar parabolic trough collector using corrugated tube receiver with conical strip inserts, Sustainability 15 (2023), https://doi.org/10.3390/su15010378.
[69] G. Hou, A. Yadav, E. Ali, Y.A. Naeem, F.F. Ahmed, K. Muzammil, K.T. Falih, H. A. Abdulridui, E.H. Kadhum, A.A. Omran, A. Elawady, Thermal performance improvement for parabolic trough solar collectors integrated with twisted fin and nanofluid: modeling and validation, Case Stud. Therm. Eng. 60 (2024) 104763, https://doi.org/10.1016/j.csite.2024.104763.
[70] R. Venkatesaperumal, K.S. Jafar, Machine learning predictions for enhancing solar parabolic trough collector efficiency with corrugated tube receivers, Sadhana - Acad. Proc. Eng. Sci. 49 (2024), https://doi.org/10.1007/s12046-024-02493-0.
[71] S. Sevim, S.K. Arabacı, A. Yurddaş, Enhancement of heat transfer performance of parabolic solar collector using a novel type turbulator, Appl. Therm. Eng. 286 (2026), https://doi.org/10.1016/j.applthermaleng.2025.129259.